Synergistic Foam Stabilization and Transport Improvement in Simulated Fractures with Polyelectrolyte Complex Nanoparticles: Microscale Observation using Laser Etched Glass Micromodels

[1]Hooman Hosseini, [1&2]Jyun Syung Tsau, [3]John Wasserbauer, [4]Saman A. Aryana, [1&2]Reza Barati Ghahfarokhi**

[1]Department of Chemical and Petroleum Engineering, University of Kansas, Lawrence, Kansas 66045, USA

[2]Tertiary Oil Recovery Program, The University of Kansas, Lawrence, KS, USA 66045

[3]microGlass LLC, 17647 Trenton Drive, Castro Valley, CA 94546

[4]Department of Chemical Engineering, University of Wyoming, Laramie, WY 82071, USA.

Correspondence to: Reza Barati Ghahfarokhi (E-mail: reza.barati@ku.edu), Saman A. Aryana (E-mail:saryana@uwyo.edu)

ABSTRACT:

Inaccessibility to direct pore scale observation in hydrocarbon recovery of tight shale formations poses a great challenge to water-energy nexus initiatives and necessitates the use of high throughput technologies to emulate environmentally friendly processes. Herein, we employ a precise glass micromodel fabrication and visualization method to isolate the supercritical CO_2 bubbles surrounded by CO_2-water lamella prepared in saline produced water stabilized with molecular complexation of zwitterionic surfactants (ZS) and polyelectrolyte complex nanoparticles (PECNP).

The Selective Laser Enhanced Etching (SLE) technique was selected for micromodel simulation of high-pressure flow. Two representative designs, (1) fracture/micro-crack network and (2) fracture/matrix were etched on fused silica glass with a laser printing machine and $scCO_2$ foam was injected to study the foamability, propagation, stability, and fluid loss properties.

The highly monodispersed and uniformly distributed array of $scCO_2$ bubbles were detected in flow of $scCO_2$ foam in highly saline brine containing ionic complexes of positively charged PECNPs and ZS, whereas foam flow with the lamella containing ZS in fractures offered a noticeably large and polydisperse array of $scCO_2$ bubbles. $scCO_2$ bubble motion and deformation were traced, and local description of foam flow was visually examined. The confined array of $scCO_2$ bubbles stabilized by ZS in microcracks was affected by bubble growth and coalescence, whereas the super-populated array of monodispersed $scCO_2$ bubbles with lamella containing complexes of PECNP and ZS were able to fill the channels with stable configurations within the timeframe of comparative stability measurements. The ability of complex fluid to prevent the formation damage was evaluated through fluid loss visualization in micromodels. Probing $scCO_2$

foam transport in homogenous porous media revealed smaller volume leak-off for $scCO_2$ foam containing PECNP-ZS ionic complexes.

KEYWORDS: "Selective Laser Enhanced Etching" "Microfluidic", "Polyelectrolyte Complex Nanoparticles", "Zwitterionic Surfactants", "Fracture", "$scCO_2$ foam", "Produced Water".

1. INTRODUCTION

Prior to the 2020 pandemic the energy sector was at the highest level of oil and natural gas production [1]. This historic boost was thanks to a combination of horizontal drilling and hydraulic fracturing of tight shale formations aiming at significantly higher production, thereby lowering hydrocarbon cost and petroleum imports [2,3]. Unconventional oil recovery techniques, such as hydraulic fracturing where pressurized fluids are injected to fracture the rock and stimulate the production from low permeability formations (permeability less than 1 mD and below 15% porosity), have become a major contributor to the liquid petroleum production from subsurface formations [4–6]. Moreover, shale formations are potential targets for CO_2 storage [4,5] as part of a global effort to limit greenhouse gas emissions and to utilize the emitted gases in environmental-friendly processes [7,8]. Examples include the use of compressed CO_2 [9] in extraction/purification processes [10,11], microelectronic processing/cleaning [12] efficient drug delivery and controlled release [13]. Additionally, compressed CO_2 has the potential to replace water in fracturing of shales [14] and to contribute to the reduction of anthropogenic carbon emissions by storing CO_2 in geological formations as part of the Carbon capture utilization and storage (CCUS) program in the United States [15,16].

Issues related to water availability, large scale water disposal leading to seismicity and earthquakes, freshwater contamination during injection/production, and formation damage

have all negatively affected the water-energy nexus in unconventional oil recovery [17,18]. Therefore, waterless fracturing using supercritical CO_2 ($scCO_2$), with CO_2 as the dispersed phase and produced water as the continuous phase (on-site disposal), is a promising path to for subsurface CO_2 storage that improves the sustainability of production life cycles of unconventional assets [5,19].

The improved mass transfer and increased selectivity of $scCO_2$ is due to its the high diffusivity (gas-like properties) and high density (liquid-like properties) [19,20]**.** Other potential benefits of $scCO_2$ in the subsurface include improved miscibility and viscosity, lessened risk of formation damage, and relative ease of recycling [14,21,22]. As such, $scCO_2$ foam (Foams, as a predominant dispersion of gas in liquids) is a prime candidate for waterless fracturing (non-aqueous phase fraction $\Phi \geq 90\%$) [14]. The stability of High Internal Phase (HIP) emulsion $scCO_2$ foam influences its ability to carry rigid proppant particles, the conductivity of the resulting fractures and hydrocarbon production [23]. Effective injection of foam in wellbores and fractures requires that lamella remain stable [14], until foam contacts the oil to allow for efficient distribution of proppants and flow back recovery prior to fracture closure [5]. The chemical composition of $scCO_2$-water lamella may be tailored to obtain such a smart HIP emulsion [14]. Since reversible shear-induced degradation and return to the original form in ZS is controlled by short relaxation times, it is an ideal candidate as a foam stabilizer for subsurface applications [20].

Synergistic ionic enhancement is additionally introduced to address detrimental impacts of foam behavior under shear and low viscosity, which affect final fracture width and height [6], and related environmental issues [5]. Foam stability and rheological properties of $scCO_2$ at gas-liquid interfaces in fractures are enhanced via the stabilizing effect of ion

active species such as zwitterionic surfactants (ZS) in form of wormlike micelles (WLMs). These WLMs contain amidopropylhydroxysultaine with a long hydrophobic tail, sulfonate, and quaternary ammonium pendant groups [14] and polyelectrolyte complex nanoparticles (PECNP). The nanoparticles comprise self-assembled counter-ionic polymers (Dextran sulphate (DS) and Polyethylenimine (PEI)) in the form of amphoteric ionomers dissolved in produced water (concentrated aqueous electrolyte comprising variety of dissociated ions in particular divalent ions) (Figure 1a, c) and may be evaluated by the lamella liquid drainage rate and $scCO_2$ bubble collapsing time obtained by macro scale studies such as dynamic foam rheology and view cell measurements [14].

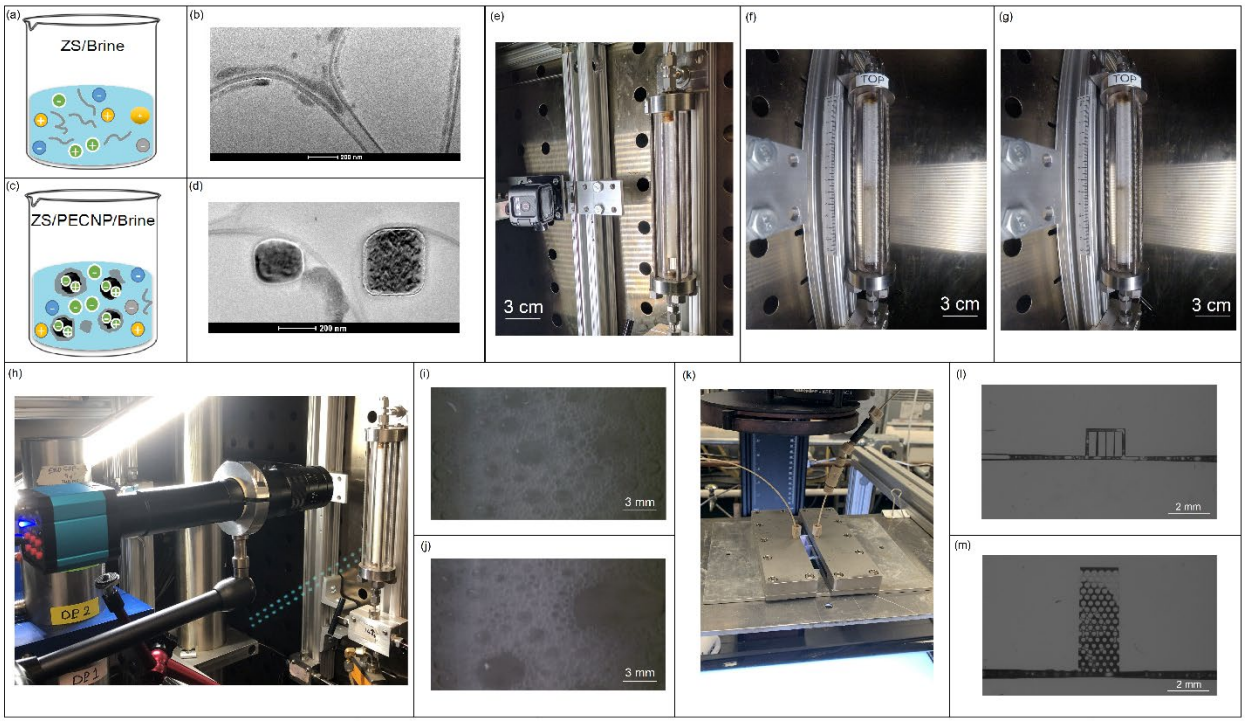

Figure 1. Variety of foam lamella constituents and resulting foam morphology in multiscale observation of complex fluid flow: (a, c) schematic of aqueous solutions containing ZS and ZS/PECNP in high saline brine (b, d) TEM images of electrolyte dispersion of wormlike micelles (WLMs) and Polyelectrolyte Complex Nanoparticle (PECNP), mechanistic details of molecular complexation is found in our previous study [14], (e) macro-

scale observations of foam texture in view cell revealing the height stability of (f) ZS generated $scCO_2$ foam and (g) ZS-PECNP generated $scCO_2$ foams. (h) Local magnification of field of view to reveal the macro scale texture of generated $scCO_2$ foams stabilized with (i) ZS and (j) ZS-PECNP complexes (k) micro scale observation of foam texture, stability, and fracture transport in two configurations: (l) fracture/micro-fracture (m) fracture/matrix.

Mechanism of this synergistic stabilization in highly concentrated brine (aqueous electrolytes) was previously studied via Raman Spectroscopy and TEM (Figure 1b, d) to establish a framework for gas-water lamella disjoining pressure enhancements in EOR and fracturing applications [7,14]. TEM images of complexes are presented in Figure 1d and a schematic of complexation is shown in Figure 2.

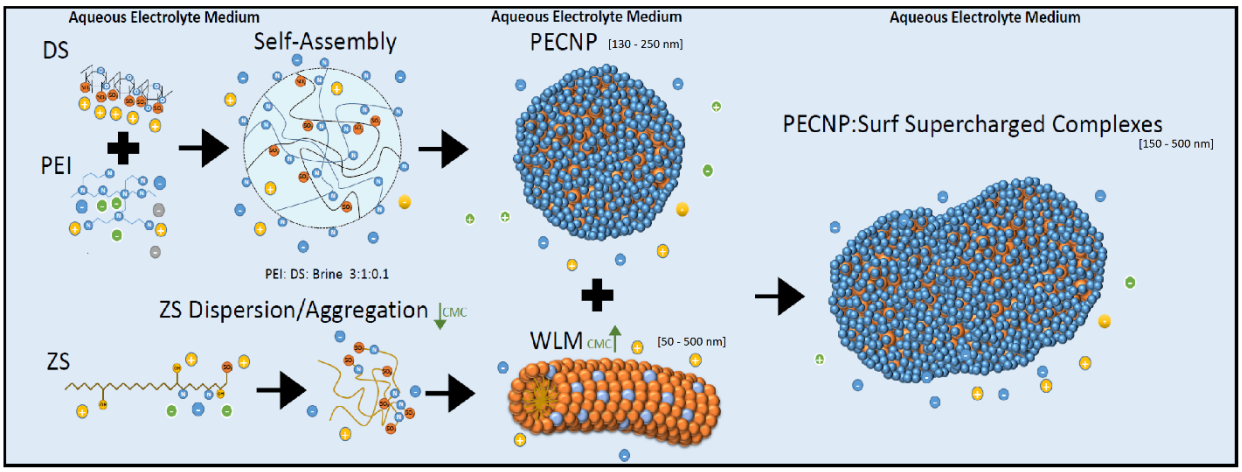

Figure 2. vesicular complex formation mechanism in highly concentrated electrolyte, The underlying mechanism was identified with TEM and Raman Spectroscopy as electrostatic rearrangement of WLMs along the structure of PECNP to form electrostatically bond layers bond layers with nanoparticles and create a stable complex [14]

The novel fracturing fluids enhanced by complexation of ZS and PECNPs improve fracture width and height, clean-up and conductivity as well as the potential for CO_2 storage and sequestration in geological formations [14,22]. However, the microscale transport and

stability mechanisms of $scCO_2$/brine systems, as well as fluid loss between fracture and matrix, are not quite understood [23]. Recent macroscale observations of complex fluid structures (Figure 1e, f, g, h, i, j) [7,14] indicate (i) an accelerated gravity drainage in vertical foam view cell which negatively affects morphological observations and (ii) a lack of complementary transport studies in simulated fractures. These observations are in agreement with the literature regarding difficulties associated with visual analysis of 3D bulk foams and the importance of microscale observations [24].

In recent years, there has been a renewed interest in experimental systems that enable direct observation of multiphase transport within geological surrogate micromodels in the context of CCUS [23]. Porter et al. used $scCO_2$ and real-rock micromodels with idealized and realistic fracture patterns to study imbibition, hydrocarbon/brine displacement and $scCO_2$-brine-oil flow within the channels [25]. Middleton and co-workers used a shale micromodel to inject $scCO_2$ into a water saturated fracture, and to observe different localized flow patterns and dissolution of $scCO_2$ in water [15]**.** These studies did not, however, focus on the stability of $scCO_2$ foams at microscale in fractured media and the assessment of the potential for formation damage. Much of the literature is centered around micro observation of displacement efficiencies and capillary fingering of $scCO_2$ or foam generation and mobility control in fractured reservoirs in the context of EOR [20,26,27] As such, there is a need for microscale studies of stabilization of $scCO_2$ bubbles in concentrated electrolytes with confined movement in fractured media for sustainable and environment-friendly (e.g., water-less) oil recovery processes.

Subsurface-emulated lab-on-a-chip (LOC) devices (e.g., figure 1l and m) provide a platform to study pore level dynamics of ionically stabilized $scCO_2$ in fractures and micro-

fractures with interconnected or dead-end topologies [23] Photolithography, wet etching and thermal bonding provide a pathway to fabricating such LOC devices [28]**.** Inadequate mechanical integrity and non-uniformity of the etched geometrical patterns due to the bonding process may adversely affect the pressure resistivity and the quality of the observations [29].

A number of relevant microfluidic platforms have been developed over the years to study various chemical and petroleum processes [30] and we have reviewed them in our previous work [31]. Most of the reports in literature that leverage microfabrication are concerned with real-time control and characterization of the hydrodynamics, sensing and in-situ chemical reactions, whereas, oil and gas relevant pore-scale observations (e.g., CO_2-EOR) with harsh reservoir condition often leave out of important fabrication details [31].

Electromagnetic radiation provides an alternative path to etch channels on glass substrates. Moreover, the advent of femtosecond (fs) laser micromachining of patterns on a variety of materials [32] using short pulse durations and energy deposition times has led to minimum damage and improved spatial resolution [33]. Structures and patterns may also be directly written using fs-lasers in bulk glass [34]. The desired pattern is directly 'laser-written' inside the glass substrate and the entire procedure (prior to wet etching) is automated [29] via the use of 3D micro scanners (fast writing of micro vectors with micrometric resolution) and precise micrometric 3-axes system [34]. Such a process eliminates the steps required for sealing the micromodel such as anodic or thermal bonding.

Perhaps main advantage of the SLE method over other techniques is that the remaining glass exhibits bulk properties. The wet-etching process does not introduce micro-cracks on the glass surface. Therefore, the pressure limit versus thickness calculation can use the bulk modulus of

fused silica. Because the laser passes through a polished surface, the SLE process can write aberration-free voxels to a depth of 10 mm.

The present study focuses on foamability, fracture transport, stability, and fluid loss behavior of $scCO_2$ in highly concentrated electrolytes (high saline brine, sea level salt concentration) containing ionic stabilizers such as ZS and complexes of ZS and PECNP in pressure resistive and simplified 2D fractured patterns of glass micro-models. The performance of dry foams stabilized with 1 wt% ZS was compared to ZS-PECNP enhanced foams containing bio-friendly and supercharged ionomer complexes. Microscale observations were made using glass microfluidics, and the findings helped correlate the physio-chemical characteristics of these foams across micro and macro scales and in the context of unconventional oil recovery. Foam texture and individual lamella resistance in different fracture geometries were determined by steric disjoining pressure enhancement originated from electrostatic complexation of surfactant oligomers and ionomers in nanoparticles. The fracture patterns were designed to simulate the geometry of the pathways that transport fracturing fluids in fractured reservoirs. The pathways may comprise simplified patterns of fractures and micro-fractures, or they may be realistic depictions based on micro-CT data. In this work, the fracture pattern was designed using CAD. Laser etching and photolithography were employed to create glass LOC devices bearing the designed network of channels. These devices were coupled with a high-resolution camera to examine in-situ generation, transport, stability, and fluid loss for dry $scCO_2$ foams. The collected data was processed to develop a physiochemical correlation between micro-facture/matrix transport and to understand the stability behavior of $scCO_2$ foams. Additionally, the ability of different ionic stabilizers (ZS and ZS-PECNP) was

assessed. The findings of this study are of value in a host of applications dealing with microscale transport and isolation of $scCO_2$ in confined media.

2. MATERIALS AND METHODS

2.1. Complex fluid preparation

High internal phase emulsion consists of $scCO_2$ foams stabilized in highly concentrated electrolyte containing surfactants and nanoparticles. Figure 3 illustrates the experimental procedure that was used to produce complex fluids and Figure 2 illustrates the underlying mechanism of ionic complexations between surfactant and nanoparticles in aqueous solution prior to mixing with $scCO_2$.

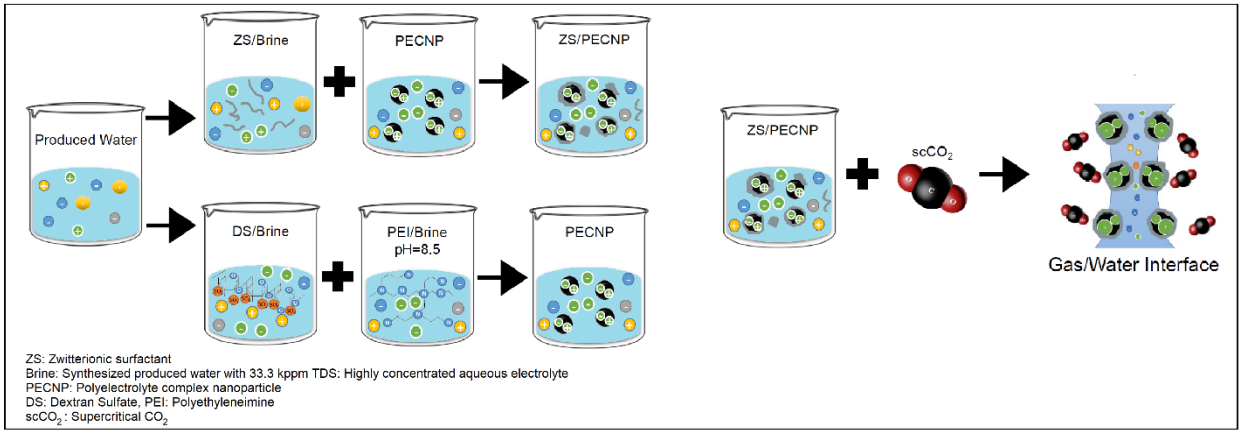

Figure 3. experimental procedure for complex fluid and gas-water interface formation

Highly concentrated aqueous electrolytes were synthesized – see [5,21] for details. The Mississippian Limestone Play (MLP) recipe contains aqueous solution of more than 202,848 ppm total dissolved solids consisting of $CaCl_2.2H_2O$ (Fisher Chemical, Certified ACS), $MgCl_2.6H_2O$ (Fisher Chemical, Certified ACS, Crystalline), $SrCl_2.6H_2O$ (Fisher Science Education, Lab Grade), Na_2SO_4 (Fisher Chemical, Certified ACS, Granular) NaCl (Fisher Chemical, Certified ACS, Crystalline) and KCl (Fisher Chemical, Potassium

chloride for calomel cells, Crystalline). These salts were dissolved in reverse osmosis and deionized water (RO- DI- water) according to enthalpy of dissolution. The salt type and concentration in MLP brine are shown in Table S1 in (Electronic Supporting Information, ESI). The highly concentrated brine was synthesized according to laboratorial recipe adopted from original MLP recipe (202,848 ppm, ~200,000 ppm), and it was diluted to sea-water salinity of 33,333 ppm (6X) nominal concentration. Zwitterionic surfactant HDP-0761-12-2AM was provided by Harcros Chemicals Inc. The surfactant structure was designed for optimum ionic activity in the form of short chain aliphatic molecules with positive amine and negative sulfonate functional groups (Figure 2). The main ingredients, i.e., solvents and additives used in the surfactant solutions, are listed in Table S2 (provided by Harcros). The ZS was dissolved in 33.3 kppm brine to form 1 w/w% reference solutions. Polyelectrolyte complex nanoparticles (PECNP) were prepared according to the procedure developed by Barati and co-workers [21,22,35]. Branched polyethyleneimine (PEI) was obtained from Sigma Aldrich with an average molecular weight of 25,000, 1.03 g/mL density at 25 °C and corresponding viscosity ranging between 13,000 cP to 18000 cP at 50 °C. Dextran sulfate (DS) was provided from Sigma Aldrich with 500,000 molecular weight. PEI and DS were separately dissolved in high salinity brines with 1 w/w% and the pH for PEI solution was lowered to 8.5 by addition of 6N HCl. The solution of 1 w/w% DS in high salinity brine was prepared and PEI and DS solutions were mixed accordingly. The mixing ratio of PEI to DS, to the diluting brine solution (PEI:DS:Brine) was chosen to be 3:1:0.1 to make positively charged nanoparticles with optimum surface charge. This ratio was developed based on previous observations with zeta potential and particle size measurements [5,14]. The nanoparticle solution was mixed with surfactant solutions (1

w/w %) in 33.3 kppm brine for 20 minutes to form the PECNP-surfactant complexes with mixing ratio of PECNP:Surfactant 1:9 (best performing ratio according to previous observations [5,14]). The concentration of the ZS surfactant remains constant when mixed with nanoparticles (1 w/w %).

2.2. Microfluidic device fabrication: Selective Laser-enhanced Etching (SLE)

network of fracture/micro channels (Figure 4).

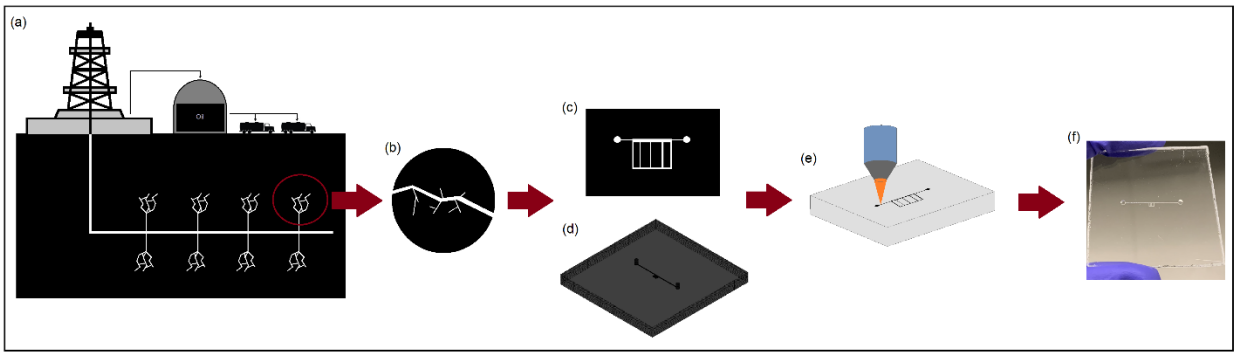

Figure 4. Emulation of fractures for SLE-based glass micromodels for subsurface oil recovery of tight shale formations (a) hydraulic fracturing of tight shale formations is considered as the target model; (b) data related to real fracture geometry from rock samples are obtained; (c, d) simplified pseudo fracture network is designed in 2D and 3D; (e) Laser printing of the pseudo fracture network in a fused glass micromodel; and (f) a completed SLE micromodel.

A pattern of fractures covering an area 127 µm in width and 2.2 cm in length was developed. The arrays of micro-cracks were all connected to the main channel – see Figure 6a. The microfractures, labelled 2 through 4 in Figure 6a, were 15.87 µm, 31.75 µm, 63.5 µm in width, respectively, while the main fracture (labelled 1, 5 and 6 in Figure 6a) was 127 µm in width. The main fracture was linked to circular inlet/outlet ports 0.04 cm in diameter. These inlets enable homogenous dispersion of multiphase fluids upon

injection/extraction. These features are all 254 μm in depth and are positioned approximately 1746 μm from one face of a 4.5 mm thick glass micromodel (Figure S2 and S3 in ESI). Following the design described above, the SLE micromodels were fabricated from Fused silica glass (SIEGERT WAFER GmbH) by LightFab GmbH, Germany. A LightFab 3D printer with a scanning focused ultrashort pulsed laser (femtosecond laser) source from Trumpf GmbH, Ditzingen, Germany was used to locally change the glass properties in the focal volume with a pulse duration of 0.5 ns, a repetition rate of 50 kHz, pulse energy of 400 nJ, and a wavelength of 1.06 μm. A linearly polarized laser beam oriented perpendicular to the stage was used to write the pattern in the double-polished fused silica. During fabrication of SLE chips, the laser beam was focused on a spot that was 2 μm in diameter. The absorption volume (voxel) was approximately 2 μm in diameter in the horizontal direction and 5 μm long in the vertical direction. The laser writes a volume pixel (voxel) in the shape of an oblate spheroid. These shapes connect to form a surface through the etching process. The surface resembles connected series of wavelets with an average roughness (R_a) of between 300 and 400 nm (in some rare occasion might peak to 1 μm). The etching rate for treated glass and untreated glass were reported as ~250 μm/hour and ~0.25 μm/hour, respectively. The time of the process for bulk etching is referred to as 'write time' during which the laser modifies a fraction of the glass substrate, which is removed during a wet etching step to form channels. For our design, a write time of approximately 5 minutes was used to generate the microchannels. Micromodels were manually singulated to an accuracy of ± 1 mm and a channel width tolerance of +/- 5 μm. During the wet etching step, a KOH 32 wt% solution at 85˚C with sonication (ultrasound) was used. The fabricated chip was pressure

tested up to 9.65 MPa during $scCO_2$ foam injection experiments. Detailed fabrication technique is found in our recent publication [31].

2.3. Optical Microscopy

OLYMPUS OLS4000, A Lext 3D measuring laser microscope was used to optically examine the pattern on the surface of the glass micromodels. The observation was performed to visually examine the top view of pattern, to measure the channel widths and to identify possible flaws.

2.4. Micro-CT Analysis

3D micro X-ray computer tomography (Xradia MicroXCT-400, Carl Zeiss Microscopy, LLC, Thornwood, New York), optimized for non-destructive imaging of complex internal structures, was employed to image geological samples and develop the desired internal structure of the chips. The instrument was equipped with 90 keV Microfocus X-ray source and 2K*2K CCD camera and an X-ray detector with a pixel resolution of about 0.3 mm and spatial resolution of less than 1 mm. The transmission X-ray imaging of the samples was performed using an X-ray tube with a tungsten anode setting of 50 kV at 8 W. 3D images were constructed with the help of the software "XM Reconstructor 8.0" (Carl Zeiss Microscopy, LLC, Thornwood, New York), using 1600 images taken at 35 sec to 40 sec exposure times per image.

2.5. $scCO_2$ foam injection/isolation experiments

$scCO_2$ foam texture, fracture transport, stability and loss properties were examined via a high-pressure foam flooding apparatus utilized along with a micromodel module, a high-resolution Phase one camera system, an illumination source. The schematic of the system is presented in Figure 5.

Figure 5. (a) schematic of high-pressure CO_2 foam injection and visualization of micromodel in laboratorial scale; the system is capable of $scCO_2$ foam generation as well as oil injection through the micromodels. Simultaneous visualization is performed using a high-resolution camera. (b) The photo of the actual setup in the lab, reprinted with permission from [31] JOVE 2020

The CO_2 and high salinity brine were compressed and co-injected at 40°C and ~ 8.6 MPa. $scCO_2$ and pressurized high salinity brine were mixed (through glass micro-bead pack and Swagelok inline mixer with 7 μm and 15 μm pore size) and directed to the micromodel that was secured inside a pressure holder. A back pressure was applied at the outlet. The initial flow rate was selected to achieve a range of foam qualities (FQ), e.g., FQ = 90% (5.4 ml/min $scCO_2$ and 0.6 ml/min brine containing surfactant/nanoparticle). After foam

304 generation was detected at the outlet, the flow rate was reduced 100 times and relatively
305 low flow rates were maintained up to 30 min to stabilize the flow inside the micromodel.
306 For stability measurements, the flow was stopped, and inlet/outlet valves were closed
307 instantly, so the multiphase fluid inside the micromodel was isolated and visual
308 characterization was executed. The microscale observations were performed with Phase
309 One IQ260 Camera mounted on DT Versa capture station manufactured by DT Scientific.
310 An LED light box placed under the device provided the required backlight luminance. The
311 images were captured, processed, and stored electronically via Capture One software
312 running on a machine with INTEL® Xenon® CPU E5-2687W v2 @ 3.40GHz, 3.40 GHz
313 (dual processors) and NVIDIA Tesla K20 Graphic Card - 706 MHz Core - 5 GB GDDR5
314 SDRAM - PCI Express 2.0 x16. At the end of the observation, the valves were opened,
315 heaters turned off and the system was depressurized to ambient conditions. The micromodel
316 was flushed with DI water multiple times. In the case of hydrocarbon injection, the
317 microfluidic device was thoroughly cleaned by injecting a brine containing surfactants and
318 nanoparticles to rinse the oil followed by injection of DI water to rinse the surfactants and
319 nanoparticles.

320 **2.6. Image analysis and post-processing**

321 MATLAB image processing tool (the MathWorks, Inc. Natick MA, USA) coupled with
322 a general image analysis tool ImageJ (an open-source Java image-processing program
323 originally developed at the National Institute of Health and the Laboratory for Optical and
324 Computational Instrumentation at the University of Wisconsin) were used to enhance the
325 quality of images, e.g., their light, contrast, and sharpness, and to obtain the average bubble
326 size and bubble size distributions for each image. The size distribution is obtained using

the following steps: i) the desired area in each image is selected; ii) the image is converted to gray scale (8-bit image type); iii) the known distance obtained from optical/microCT observations is entered into ImageJ with 'Set Scale'. FFT Bandpass Filter command filters large structure down to 160 pixels; iv) "Adjust Threshold" is employed to create the black and white contrast between the two phases. By checking "over/under", the contrast is varied in a green and black coloured background and on B&W the ultimate black and white contrast is set; and v) using "Analyze particle" with a size range of 1 to infinity and selecting to show the overlay, the summary of particles and particle size distribution is obtained. These quantification steps are also shown in Figure S5 in ESI.

3. RESULTS AND DISCUSSION

3.1. Fracture network properties

The main model for fracture/micro-crack emulation used in this work consists of a main fracture and a regular pattern of micro-cracks with determined apertures illustrated by optical/laser microscopy in Figure 6a. The design may also include a main fracture connected to an array of circular pins to increase the flow resistance and to simulate fluid loss in tight shale formations - see Figure 6b.

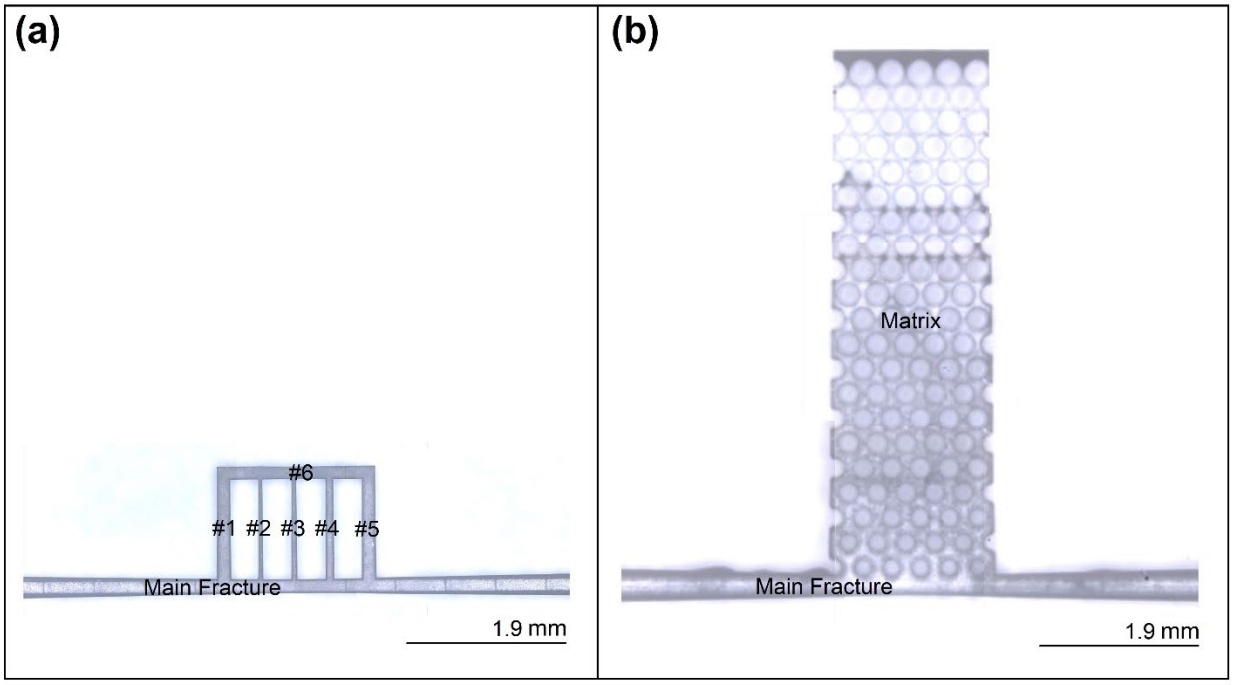

Figure 6. A close view of superimposed optical micrographs for (a) pseudo fractured network (b) fracture/matrix etched with SLE technique on fused silica.

In fracture network design #1 (Figure 3a), the largest aperture belongs to the main fracture (173.23 μm) which distributed the flowing phases through the array of micro-cracks with smaller apertures (down to 45.26 μm). For fracture/matrix design #2 main fracture aperture is 178.49 μm wide and is connected to a matrix with cylindrical grains that have an average diameter of 202.66 μm. Table 1 lists the fracture/matrix network dimensional properties for the two micromodel designs. Micro-CT validated the accuracy of reactive etching for SLE fabrication with a negligible degree of error (Figure S5 and S6 in ESI).

Table 1. Physical and dimensional properties of pseudo-fracture network (design #1) and fracture/matrix (design #2) on glass micromodel. The measurements were made by optical microscopy and micro-CT analysis.

Feature in Network (Design #1)	L (μm)	H (μm)	W (μm)	K (D)	d_H
Main Fracture (limited length in field of view as shown in Figure 6a)	6509.18	297.1	173.23	1,290	66.09
Micro-crack #1	1166.24	282.67	168.3	-	-
Micro-crack #2	1189.98	282.67	45.26	-	-
Micro-crack #3	1189.98	282.67	60.86	-	-
Micro-crack #4	1178.08	282.67	96.93	-	-
Micro-crack #5	1189.98	282.67	167.53	-	-
Micro-crack #6	1880.20	282.67	150.9	-	-
Fracture/Matrix (Design #2)	L	H	W	K (mD)	d_H
Main Fracture (limited length in Figure 6b)	6842.38	336.9	178.49	1369.82	66.75
Matrix (pinned area)	6271.18	342.67	1832.564	306.86	-
Matrix (pore throat)	-	342.68	135.1	-	-
Matrix (grain)	202.66	342.66	202.66		-

Hydraulic aperture was measured by injection of DI water and recording the injection pressure. Flow rate is related to the pressure gradient in a single fracture as [36,37].

$$\boldsymbol{Q} = \frac{\mathbf{1}}{\mathbf{12}}\frac{|\boldsymbol{\nabla P}|\boldsymbol{w}\boldsymbol{d}_{\boldsymbol{H}}^{\mathbf{3}}}{\boldsymbol{\mu}} \quad (1)$$

where Q denotes volumetric flow rate, $|\boldsymbol{\nabla P}|$ represents the pressure gradient, w is fracture width and d_H and μ are hydraulic aperture and viscosity of fracturing fluid, respectively. The pseudo-linear relation between fluid pressure and flow rate is illustrated

366 in Figure S7 in ESI. A near linear relation between pressure gradients. and flow rate points
367 to negligibility of the inertial force and variations in the aperture [36]. A slight deviation
368 from the linearity indicates minor changes in aperture during flow due to the presence of
369 main features (micro-cracks/matrix) etched near the middle of the micromodel. The aperture
370 was slightly widened for Design #2 (66.75) indicating the presence of the matrix in the
371 fracture flow pathway. The permeability of each fracture/macro-crack/matrix pathway was
372 calculated according to Darcy's equations [14], as

373 $$K = \frac{\mu.Q.L}{A.\Delta P} \quad (2)$$

374 where K is permeability of the medium (mD), μ is the viscosity of the complex fluid
375 (cp), Q is the volumetric flow rate of $scCO_2$ foam (ml/s), L is the feature length, ΔP is the pressure
376 difference across the medium, and A is the cross-section area of the fluid pathway through the
377 channels of fracture/micro-crack/matrix (cm^2). The Darci law here is used as a mean to compare
378 the permeability of medium. Permeability values for the two designs are reported in Table 1 (see
379 Table S3 for additional details). Even though the value of matrix permeability is not within the
380 range of tight shale formations (0.15 mD [14]), it is significantly lower than the permeability of
381 the main pathway (main fracture) and the ratio of matrix permeability to that of the fracture in
382 model #1 is 2.37E-4. This ratio indicates that there is a dramatic permeability change between the
383 fracture and the matrix, and that resistance to flow increases sharply as the fluids enter the matrix.
384 Fracture conductivity (F_c) was obtained from equation (3) by finding the product of fracture
385 permeability and fracture width, as

386 $$F_c = K.W. \quad (3)$$

387 F_c was found for the main fracture (0.73 D.ft). Aspect ratio, defined as the ratio of the height of
388 the channel (H) to its width (W), is a critical factor [38]. In this work, channel dimensions are

chosen such that their aspect ratios are larger than one ($\alpha = H/W$), a value that is not recommended for PDMS microfluidics due to lack of channel mechanical integrity [38]. The overall size range agrees with stimulated hydraulic fractures reported in the literature; for example, Li et al. employed $scCO_2$ to induce hydraulic fractures on homogenous and layered tight sandstones in laboratory triaxial fracturing experiment and stimulated a shattered zone with main fractures up to 348 μm wide and micro-cracks ranging from 0.2 to 92 μm in width [39]. The comparison of UV lithography chip with SLE chip in terms of design and performance is included in ESI (Figure S8 and Table S4 and S5).

3.2. Dry $scCO_2$ foam generation

Pumping a particle-laden fluid in perforated rock with low permeability exerts a shear force on the fluid not comparable (much lower shear rate [40]) to the shear history the fluid experiences while it is pumped through the wellbore tubular [14,41]. Thus, injection of the components of $scCO_2$ foam inside fractures (pre-foam generation) and real-time monitoring of multiphase flow in the formation would help elucidate the transport, shear resistivity, stability, and proppant release capability of complex fluids in fractures. $scCO_2$ foam pre-generation involves the transition of single to multiphase flow while propagating inside the main fracture and micro channels. Figure 7 illustrates multiple stages of $scCO_2$ foam pre-generation in high flow rates and a foam quality (FQ) of 90% in the SLE micromodel.

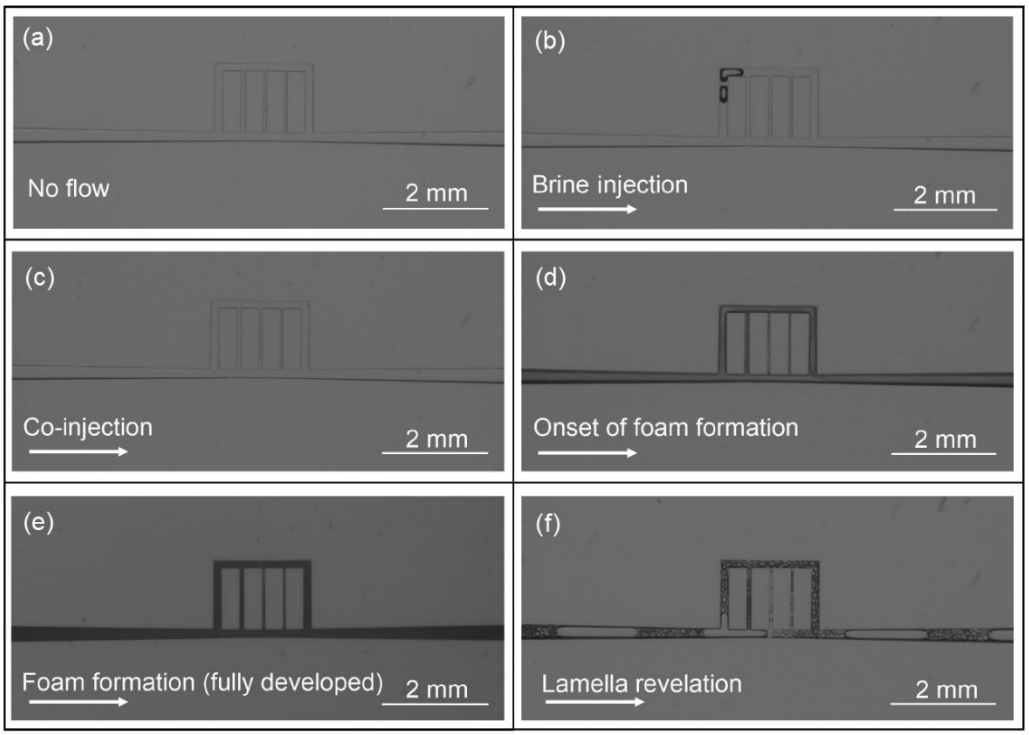

Figure 7. schematic of ZS enhanced $scCO_2$ foam pre-generation in the SLE micromodel: (a) Ambient conditions with no flow through the micro-channels; (b) injection of brine containing surfactants in the channel moves the air bubbles within the pattern (ambient conditions); (c) co-injection of CO_2 and the aqueous phase (containing surfactants or nanoparticles) at supercritical conditions (7.72 MPa and 40 ˚C) and at a total superficial velocity of 1.94 m/s; (d) onset of $scCO_2$ foam generation 5 min after the start of co-injection (8.35 MPa and 40 ˚C); (e) fully developed $scCO_2$ foam at high flow rates, 6 min after the start of co-injection (8.41 MPa and 40 ˚C); and (f) lowering the total superficial velocity to 0.019 m/s helps reveal dispersed $scCO_2$ bubbles separated by lamella in aqueous phase (8.41 MPa and 40 ˚C).

The 2D geometrical pattern with no direct flow inside the pattern is shown at ambient conditions in Figure 7a (referred to as the background). Subsequently, ZS containing, high salinity brine (33.3 kppm) was introduced to the channel at ambient conditions. As shown in Figure 7b, moving air bubbles are clearly visible upon onset of liquid pressurization. Co-injection of brine and $scCO_2$ at 7.72 MPa and 40 ˚C made no visual difference compared to the background since a recognizable multiphase flow was not formed at this stage (Figure

7c). Five minutes after inline mixing of the two phases (at inline filters, Swagelok with 15 and 7 μm pore size placed before the micromodel inlet), the grey phase was detected within the flow pathway (Figure 7d) as gas-liquid lamella started to form at this stage. The grey phase turned dark as mixing of two phases continued to create more lamella and led to a relatively uniform and homogenous multiphase case (Figure 7e). The fully developed foam was observed at the outlet of the micromodel at this stage (6 min from the start of the co-injection). Fast fluid transport (1.94 m/s) was required at initially to create and stabilize a high internal phase emulsion and once the homogeneity was achieved, the superficial velocity was reduced by 100 times to 0.019 m/s to detect the dispersed phase isolated by lamella interface (Figure 7f). Therefore, dispersed $scCO_2$ bubbles and a continuous electrolyte phase containing ionic stabilizers (ZS) were recognizable within the simplified fracture pattern.

3.3. $scCO_2$ volume fraction effect on fracture transport

Minimal fresh water use and produced water disposal are core pillars of environment-friendly hydraulic fracturing [5,19]. Therefore, establishing a sustainable water-less process highlights the effect of the gas/liquid phase volume ratio on foam stability and transport in subsurface formations [42]. It is commonly acknowledged that foam viscosity and texture are mainly controlled by FQ as the behaviour of wet and dry foams differ in terms of bubble dispersion, interaction and frictions [3]. Recent studies of foams formed near the ultra-dry limit (90 v/v% $scCO_2$ phase) indicate that these foams yielded significant viscosity improvements and fluid loss reductions in macro scale fluid transport observations [14,43]. Significant differences in flow pattern and bubble size were observed with alternation of $scCO_2$ volume fraction, as shown in micrographs presented in Figure 8.

Varying superficial velocities of $scCO_2$ and stabilizing the solution had a significant impact on the quality and texture of the foam.

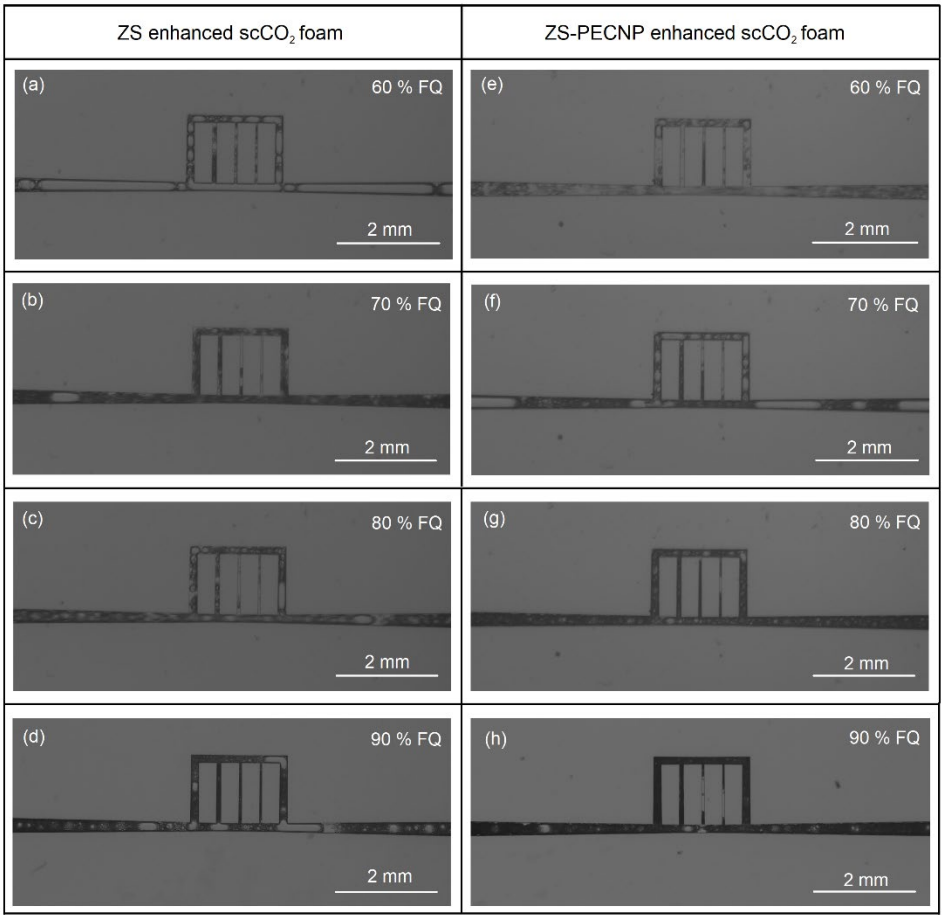

Figure 8. Comparison of foam quality at fixed injection velocities for $scCO_2$ foams generated in the fractured network: (a-d) ZS containing $scCO_2$ lamella in 33.3 kppm brine, and (e-h) ZS-PECNP containing $scCO_2$ lamella in 33.3 kppm brine.

For all the obtained patterns (FQ = 60 To 90%) the flow is not identified as segregated due to the homogeneity of the dispersion, uniform mixing verified by shear resistance properties presented in our previous observations [14,22]. In addition, the absence of gravity segregations in the micromodels may contribute to the foam flowing in threads of free gas and foam slugs [44]. For all FQs, bubble shape remained round;

however, FQ of ultra-dry foams ($\varphi > 90\%$) was not tested. Achieving a complex fluid with single uniform phase would be ideal for fracture opening and optimum proppant distribution [14]. Injection of a lower quantity of the internal phase (60 v/v%) led to formation of millimetric bubbles in the form of free gas threads in ZS stabilized foam (Figure 8a) as opposed to a nearly phase-inverted foam with a similar FQ containing ZS-PECNP enforced lamella (Figure 8e). Changing the FQ to higher volume fractions of injected $scCO_2$ phase (FQ = 70%) led to the development of a wetted foam stabilized with ZS (Figure 8b) and a dryer foam with large bubbles stabilized with PECNP-ZS (Figure 8f). Subsequent increase in the proportion of the internal phase (FQ = 80%) led to entrapment and cumulation of $scCO_2$ bubbles in the highly concentrated electrolyte solution (Figures 8c and 8g). Formation of more CO_2-water lamella with smaller bubbles was observed for ZS-PECNP stabilized $scCO_2$ foam (Figure 8g). This is in line with our previous bulk studies indicating that the addition of PECNP resulted in a more viscous and more stable foam [7,14]. Plug flow of a foam with a fully developed texture is observed in Figures 8g and 8h for ZS-PECNP stabilized $scCO_2$ foam, while ZS generated a $scCO_2$ foam with high FQs (Figures 8c and 8d) with a major fine texture with sparse dispersion of noticeably large bubbles. Cumulation of $scCO_2$ bubbles was frequently observed for higher values of FQ and for both ionically stabilized mixtures. The increase in the amount of liquid film per unit length is a result of formation of multiple electrostatically stabilized lamellas and is directly responsible for the rise in the apparent viscosity [45]. It's been reported that the foam elasticity improves with higher values of FQ (i.e., drier foams) as a contributing factor to the foams' capability to transport proppant [46]. It has been demonstrated that an improved viscoelasticity is achieved with more solid- like gas-water interface stabilized by

nanoparticle and surfactant complexes in shear thinning studies for laminar flow of incompressible $scCO_2$ foam through a Couette geometry rheometer [7,14]. Furthermore, a higher FQ may lead to a higher viscosity and reduced fluid loss to the matrix [47] (read section 3.6). One may conclude that the closely packed monodispersed arrays of bubbles in ZS-PECNP $scCO_2$ foam with a 90 v/v% gas volume fraction is an ideal candidate to optimize the foam's transport behaviour and its ability to carry and distribute proppants in fractures.

3.4. Dry $scCO_2$ foam fracture transport

Characteristics of foam flow in fractures is of importance for tight and low permeability reservoirs, since fractures are the main flow pathway of complex fluid [45]. Figures 9a and b reveals the $scCO_2$ foam produced with ZS and ZS-PECNP complexes dissolved in 33.3 kppm high saline brine upon reaching a slow momentum with low superficial velocities (0.017 m/s for $scCO_2$, 0.002 m/s for aqueous phase). An FQ equal to 90% was selected for comparative analysis, due to its optimal texture (Figures 8d and h).

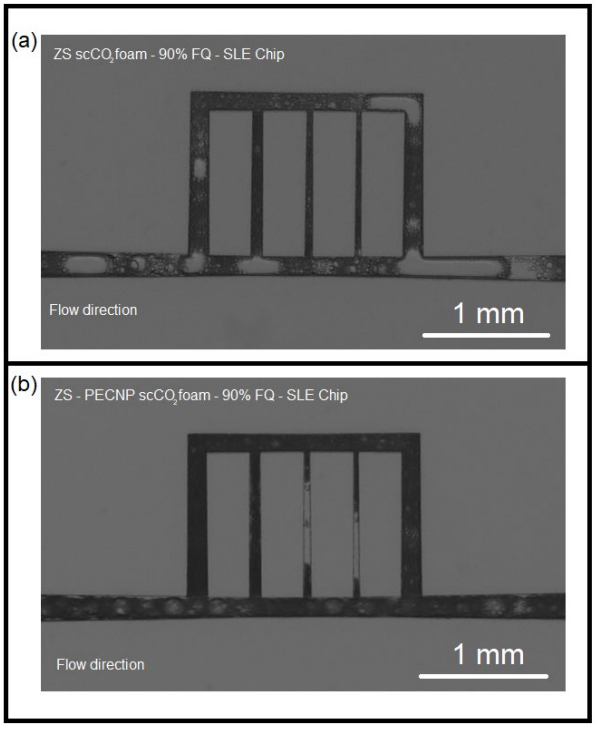

493

494 Figure 9. A dry scCO2 foam (FQ = 90%) generated within the main fracture and micro-crack after the flow with low
495 flow rates reaches the pseudo laminar stage: (a) bubble lamella stabilized with ZS in 33.3 kppm brine, and (b)
496 bubble lamella stabilized with ZS-PECNP in 33.3 kppm.

497 Larger bubbles were formed within the ZS generated foam with an average size of 40.74
498 μm and the largest size of 1028.27 μm. As a result, a coarse texture was observed, whereas
499 the largest detectable bubble sizes during coherent and stable flow of ZS-PECNP stabilized
500 $scCO_2$ foam were 137.85 μm, with a detectable average bubble size of 35.42 μm
501 representing a fine-textured foam. Table 2 lists the microstructural quantification of two
502 flow regimes in pseudo-fractured media.

Table 2. Microstructural quantification of complex fluids flowing through the fracture and micro crack (analysis was performed on detectable phases)

Foam mixture	Mean bubble size (μm)	Largest bubble size (μm)	$scCO_2$ bubble morphology	Polydispersity Index (PDI)
ZS $scCO_2$ foam	40.74	1028.27	Near to coarse	7.87 (highly polydisperse)
ZS-PECNP $scCO_2$ foam	35.42 (detectable)	137.85	Fine	2.00 (near uniform)

The bubble population in ZS-PECNP generated foam is the result of its excellent lamella formation and the stability of electrostatically enhanced foam systems. The instability of ZS-lamella upon foam generation and isolation of $scCO_2$ bubbles led to a higher bubble coalescence and lamella drainage and formation of larger bubbles upon the onset of mixing (Figure 9a). On the other hand, ZS-PECNP generated $scCO_2$ foams exhibited condensed and populated arrays of smaller and monodispersed bubbles with barely recognizable mid-sized bubbles in the smallest micro channels (Figure 9b). Fast inter-bubble diffusion/compression (no collusion) regulates the bubble size in ZS-PECNP $scCO_2$ foams propagated through the main fracture; bubble dynamic has been introduced and investigated as an influencing factor on bubble geometry in the literature [36].

Previously, it was reported that the electrostatic complexation of ZS and PECNP improves the lamella disjoining pressure and repulsive forces over the capillary pressure and van der Waals mechanisms responsible for bubble degradation and expansions [14,48]. Ostwald ripening rate is slowed down by the high packing efficiency of WLMs [49] and the effect is improved by the PECNP conjugation to WLM [14]. The improvement of the

ionic strength for aqueous polyelectrolytes is responsible for the appearance of more populated arrays of smaller $scCO_2$ bubbles. This indicates more lamellas were formed in ZS-PECNP generated $scCO_2$ foams and larger volume of foams were generated with better foamability using ZS-PECNP complexations with a constant concentration of surfactant.

Both mixtures successfully entered micro-cracks as wide as 45 μm, which illustrates the high efficiency of multiphase fluid propagation and fracture invasion to maintain pathway conductivity in the presence of a range of sizes in hydrofractures [50]. Foams were successfully diverted in cross flow from high permeability to low permeability areas and withstood the high-pressure build-up upon entering the micro-cracks. For ZS generated $scCO_2$ foams, the dispersed phase size was controlled by the width of the flow pathway under a constant flow rate (0.019 m/s). The stability of bubbles was not affected between the main fracture and micro-cracks for both stabilizing mixtures (Figure 9). ZS generated $scCO_2$ foams successfully and filled the smallest channel sizes (45 μm channel width for micro-crack #2). The PECNP-ZS generated $scCO_2$ foams, however, were unable to fill channels #2 and #3 (45, 60 μm in width, respectively) entirely. A high frequency of lamella formation resulted in a lower bubble size and a higher internal pressure led to a faster transport and rate of diffusion for ZS-PECNP $scCO_2$ foams. It also negatively affected micro-crack storage capacity and foam propagation into short-range micro-cracks (Figure 9b).

Slower transport for ZS generated $scCO_2$ foams allowed for effective tracing of the movement of singular bubbles in the network. An analogy between with the movement of a race car on the track may be used for energy loss during multiphase flow [51]: if flow carries a high momentum, it loses energy in turns and morphology and integrity are

affected. Figure 10 reveals the bubble flow direction through the fracture and channel network for lamella stabilized with ZS. Bubbles in plug flow broke upon meeting the first T-junction and fed the smaller bubbles to the micro-crack network as foam propagated through and filled the smaller channels. The movement of bubbles between smaller and larger channels may be examined in terms of stability when the flow experiences a pressure drop.

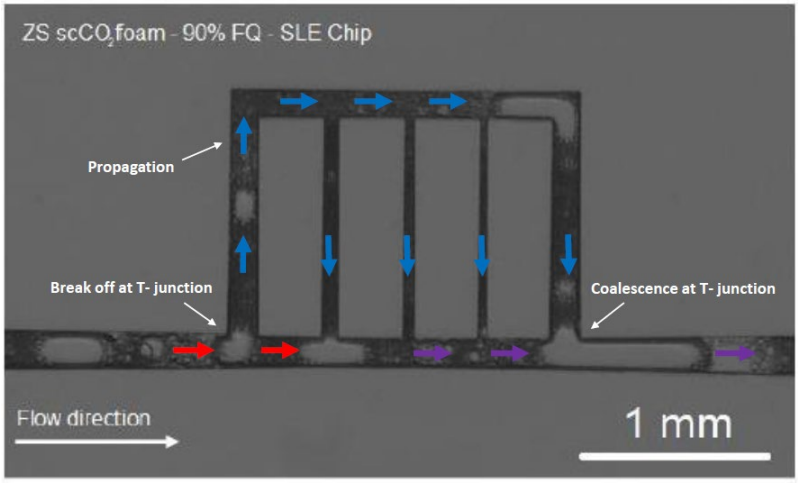

Figure 10. $scCO_2$ bubble direction through the fracture and channel network for ZS $scCO_2$ foam flow in SLE micromodel.

The morphology and integrity of ZS-PECNP generated $scCO_2$ foams were not affected by flow divergence from micro-cracks to the main fracture, whereas the bubble growth and coalescence at T-junction was observed for ZS generated $scCO_2$ foams (Figure 10). This indicated that the $scCO_2$ lamella became unstable around sharp edges and when lamella was only filled with WLMs. Conversely, confinement and flow divergence did not induce deformation in bubbles and breakup of fluid interface comprising ZS-PECNP complexes. Flow of ZS-PECNP foams in the main fracture and the network of micro-cracks remained stable for a relatively long period (Figure 11). Inability to fully examine the texture of ZS-

PECNP $scCO_2$ foams was in part due to a high lamella formation and the high degree of droplet monodispersity. This prohibited a reliable analysis of bubble population. Instead, we generated foams at macroscale and observed using a view cell (Figures 1i and 1j). To characterize the dynamics of $scCO_2$ foam bubbles, dimensionless parameters, namely Reynolds, Peclet, Stokes and Capillary numbers are used to capture information about the microstructure, shear condition and relative density [46]. These parameters help explain the foam hydrodynamic dependence on the microstructure (Table S6 in ESI). To calculate basic hydrodynamic parameters, results from macro scale observations were considered (see Figures 1h – j, and Table 3). Macro scale observation was performed on visualized flow of $scCO_2$ foams generated in standard 1/8 inches stainless steel pipes. The shear rate was calculated according to the velocity distribution profile for power-law flow in circular pipes [52]. Refer to Tables S7 and S8 in ESI for more details.

Table 3. Dimensionless parameters to characterize the dynamics of bubbles in $scCO_2$ foam (T=40 °C, 313.15 °K, K_b = $1.38064852 \times 10^{-23}$ m^2 kg s^{-2} K^{-1}, $\varsigma = 1$) FQ = 90 %

Parameters/33.3 kppm System	ZS $scCO_2$ foam	ZS-PECNP $scCO_2$ foam
$\mathbf{R_b}$(μm)	144.76	102.62
$\boldsymbol{\mu_m}$**(cp)**	1	1.05
$\dot{\boldsymbol{\gamma}}$ (1/s)	26.30	31.74
$\boldsymbol{\rho_m}$ (gr/cm^3)	1.0217	1.0221
$\boldsymbol{\rho_b}$(gr/cm^3)	0.526	0.526
Σ (mN/m)	6.355	6.43
Re	56.32	32.54
Pe	3.48E+8	1.57E+8
Stk	4.2E-3	1.7E-3
Ca	6E-4	5.3E-4

Table 3 shows the values of the dimensionless parameters using the average bubble diameters obtained from macro visualization experiments (Figures 1h – j). Values of Reynolds number, defined as the ratio of inertial to viscous forces, suggests that the flow regime for all stabilizing mixtures was laminar (Re<2300). This illustrates the homogeneity of phase dispersions and a lack of eddies at moderate flow rates in small tubes [53]. Relatively high values of Peclet number indicates that slow bubble movements overcame Brownian movements and that hydrodynamic interactions were prevalent. Low values of Stokes number ($Stk \ll 1$) showed that no phase segregation occurred in $scCO_2$ foams (FQ = 90%) [46]. Capillary number is a measure of bubble deformity [46]; at early stages of deformation and at low values of capillary number, the emulsion is isotropic [46]. Capillary number has a correlation with bubble deformation under shear, so it represents destabilizing forces in the lamella as well as the magnitude of opposite forces to disjoining pressure. In the case of ordered foams, the packing structure of the bubbles is dictated by capillary pressure and surface energy minimization [46]. As such, improvements in disjoining pressure through electrostatic interactions balances the forces in CO_2-water interfaces, and the capillary value decreases for ZS-PECNP generated $scCO_2$ foams (Table 4).

The propagation of $scCO_2$ foam for both ZS and ZS-PECNP mixtures are shown in Figure 11.

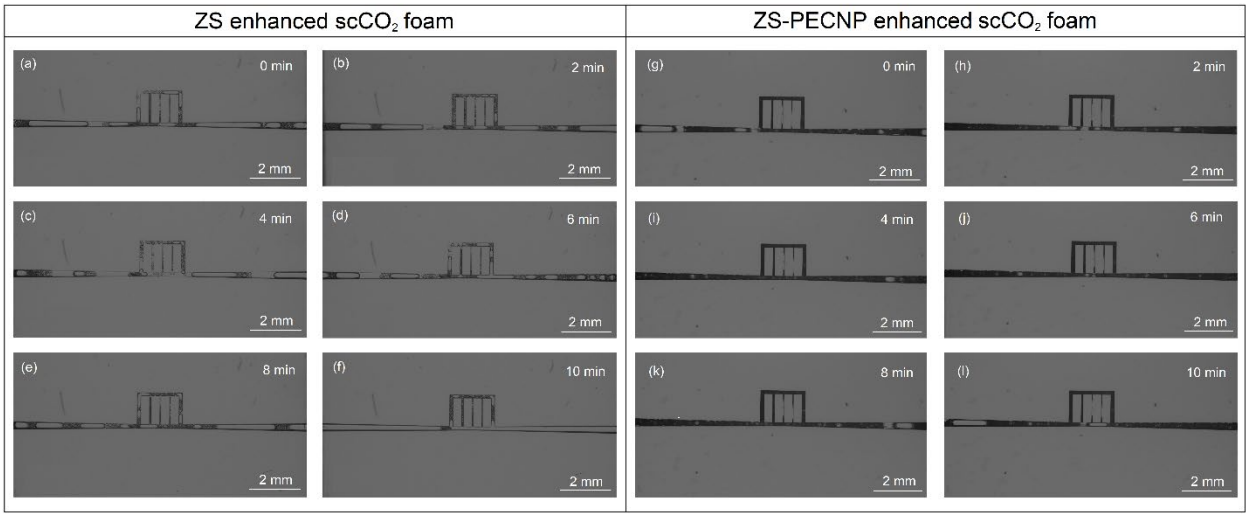

592 Figure 11. $scCO_2$ foam propagation schemes in chronological order for scCO2 bubble in highly saline brine (FQ =
593 90%) containing (a-f) ZS and (g-l) ZS-PECNP mixtures.

594 The transport of $scCO_2$ foams through the fracture slit is shown in Figure 11. The fluid
595 total superficial velocity was 0.019 m/s. The prominent feature of ZS-generated $scCO_2$
596 foams was the movement of rather large bubbles of $scCO_2$ surrounded by interconnected
597 arrays of smaller $scCO_2$ bubbles dispersed in highly saline brine (Figure 11a). At early
598 stages of transport (Figure 12b, t = 2 min), the flowing phases appeared segregated in the
599 main fracture, even though flow was homogenous in the micro-crack network. At later
600 times, the flowing phases became segregated throughout (Figure 11c to 11e) and eventually
601 a $scCO_2$ filled the main channel (Figure 11f, t = 10 min). This phenomenon is attributed to
602 the instability of CO_2-water lamella leading to bubble growth, coalescence, and ultimate
603 instability of the multiphase transport. Bubble growth and coalescence directly affects
604 proppant settling rate and triggers fast sedimentation [54]. Zhu et al. argued that for unstable
605 lamella, the plateau border is unable to provide the drag force against gravity in shale
606 formations due to a reduction of bubble pressure [55]. Therefore, a deficient proppant
607 settlement is expected for ZS generated $scCO_2$ foams. Consistently textured foam was

608 observed in the case of ZS-PECNP generated $scCO_2$ foams (Figure 11 g to 11 l). The slugs
609 of $scCO_2$ were smaller (detectable up to 35μm), although channel filling (micro crack
610 network) was not as effective as in the case of foams generated with WLMs. In ZS-PECNP
611 generated $scCO_2$ foams, high shear rates in narrower micro-cracks had a negative impact
612 on consistent foam transport throughout the system [46]. The distribution of phases with
613 supercharged ionic complexes in aqueous phase was relatively uniform during the time
614 frame of fluid invasion of micro-cracks (10 min). Micro-cracks with smaller dimensions
615 than main fractures (up to 4 times smaller, see Table 1) induce larger pressure gradient and
616 may locally strain the stability of the foams due to topological changes [56]. The pressure
617 drop through the micro channel network did not, however, appear to adversely affect bubble
618 size and phase stability in the observations. It was previously reported that ZS-PECNP
619 $scCO_2$ foams offer higher apparent viscosities compared to ZS foams in the range of shear
620 rates experienced from wellbores to fractures [14]. Higher shear resistivity leads to the
621 formation of smaller bubbles and narrower size distribution [46]. This is mainly due to the
622 ability of ionic complexes to improve storage capacity of interfaces against the
623 deformations [46]. The observations are consistent with previously measured flow
624 consistency index K= 2916.4 $Pa.s^n$ for ZS-PECNP foams versus K=1184.3 $Pa.s^n$ for ZS
625 based $scCO_2$ foams in the studied shear rate range (Figure S9 and Table S7 in ESI). These
626 observations verify an improved capability of complex fluids to transport proppants
627 [14,57] and undergo elastic deformations in constrictions [56].

628 **3.5. $scCO_2$ bubble stability in main fracture**

629 Selection of proper fracturing fluids has a direct impact on the resulting fracture width,
630 fluid loss, fracture conductivity and fracture clean-up process [14]. Failure to maintain foam

stability results in an inhomogeneous distribution of proppants in the fractures [10]. $scCO_2$ foam stability in the fracture may be affected by high temperature conditions, high shear rates during the pumping stage and low shear rates while fracture is closing [10] . Stability of ZS and ZS-PECNP generated $scCO_2$ foam was compared over a period of 120 min from the point the multiphase flow was stopped, and the micromodel was isolated. The micrographs are illustrated in Figure 12.

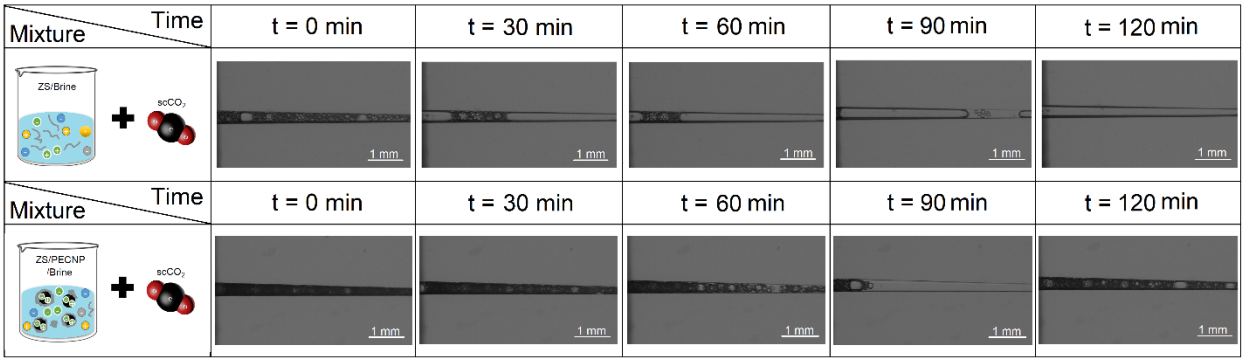

Figure 12. Foam stability comparison in the main fracture, starting from when flow was stopped, and micromodel was isolated.

The stability of $scCO_2$ foams generated using ZS along the main fracture was drastically affected by bubble coalescence and lamella breakage during the first 30 min of stabilization. The lamella was not stable enough to separate the $scCO_2$ phases from each other in the electrolyte solution. For ZS-PECNP generated $scCO_2$ foams, extremely small and monodispersed droplets were largely stable in the fracture slit for the entire duration of the experiments, except for infrequent unstable movements at t = 90 min, attributed to inertia effects. Some gradual bubble growth was observed but these effects were not significant to destabilize the overall stream. ZS-PECNP $scCO_2$ foams remains stable for during the entire time frame of isolation (up to 7 hr – Figure S10 in ESI).

3.6. $scCO_2$ bubble stability in micro-cracks

Figure 13 illustrates the level of stability for $scCO_2$ bubbles in micro-crack networks. The main foaming solution fed the micro-cracks from the main channel positioned at the lower edge on the field of view.

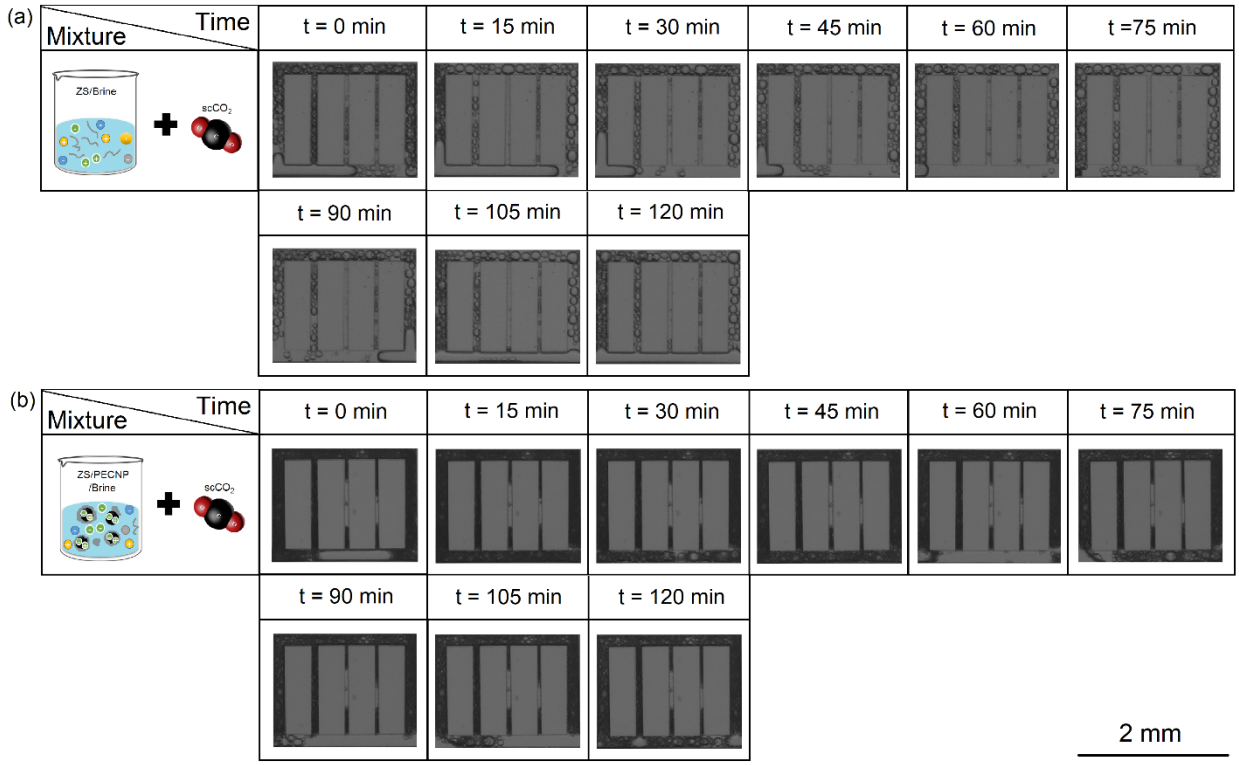

Figure 13. Stability of foaming mixtures in the network of micro-cracks for scCO2 bubbles stabilized in high salinity electrolytes containing (a) ZS, and (b) ZS-PECNP, in 15 min increments after foam isolation in the SLE micromodel.

Movements of bubbles was visible in ZS generated foams (Figure 13a). Initially the bubbles in the main fracture entered the micro-cracks by breaking into smaller bubbles within the aperture of the micro cracks. Foam within the micro-cracks was stable throughout the experiments (t = 2 h). Local variations in bubble size were observed as bubbles traveled and collided with the single millimetric bubble (Figure 13a, after t = 105

min). Despite the isolation of the micromodel from the inlet and the outlet, the inertia in the channels resulted in bubble movement and relocation. Highly monodispersed and emulsified $scCO_2$ foams with lamella containing ZS-PECNP complexes successfully maintained their stability and resulted in high channel occupancy (Figure 13b). The mixture remained stable for the entire time frame of isolation (up to 7 hr – Figure S11 in ESI). This was mainly due to surfactant-brine solubility and nanoparticle compatibility to the WLMs and concentrated electrolytic interface.

3.7. Fluid loss assessment in fracture/matrix

High internal fracture conductivity and control of the leak-off rate to the formation reduce pumping costs and ensure the mechanical integrity of the formation in an environment-friendly oil recovery process [14]. Limiting the leak-off extends the fracture length in practical operations due to higher viscosities [58]. Damage in tight and shale formations may be evaluated as a simplified 2D flow in the matrix. The schematic of this design is shown in Figure 6b and the dimensional analysis is provided in Table 1. The fluid loss assessment was performed for the flow of $scCO_2$ foams in fracture/matrix (design #2) with a high total superficial velocity of 1.66 m/s to distinguish the fluid pattern and to highlight the colour contrast in tight and shale formations. Figure 14 presents the fluid loss micrographs for ZS and ZS-PECNP generated $scCO_2$ foams from the main fracture to the matrix with an average pore throat size of 135.10 μm (micromodel design #2; see Table 1) within the first 2.5 min after foam generation. The efficient electrostatic conjugation of ZS and PECNP creates a reliable nanoparticle additive to control the formation damage in micro-scale.

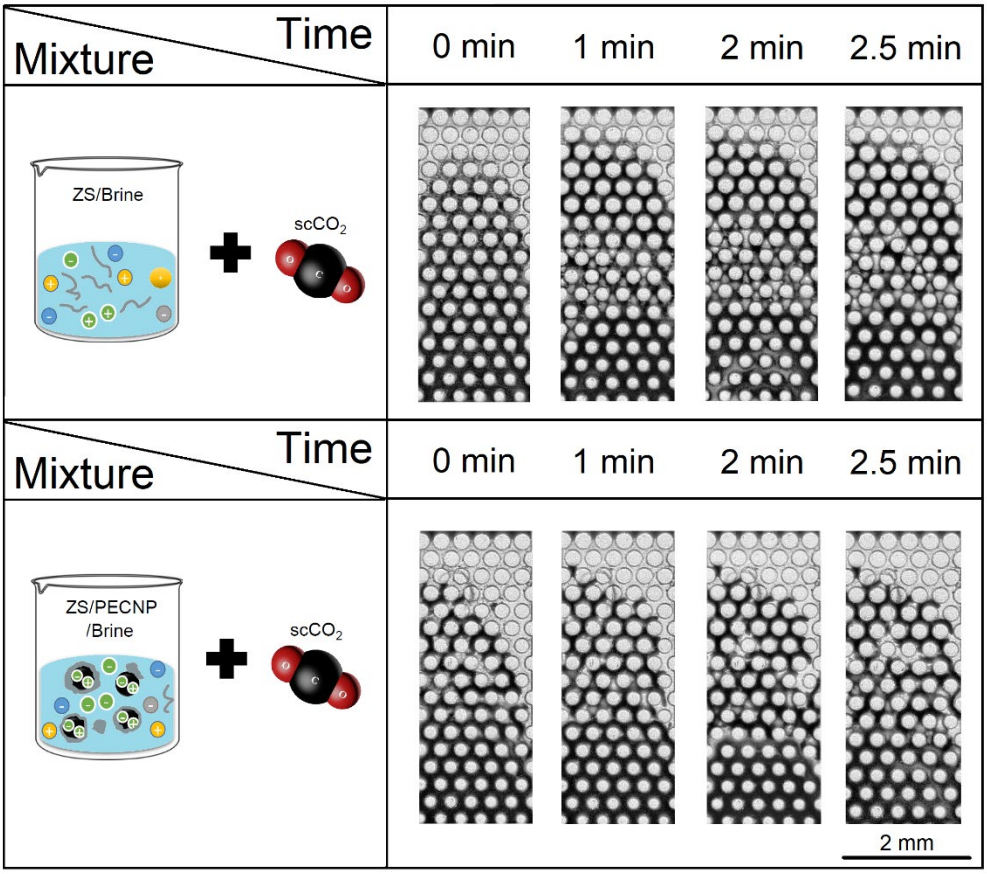

685

686 Figure 14. Fluid loss patterns (chronological binary graphs) representing leak off from the fracture to the matrix on
687 SLE micromodel design #2 (top row) flow of ZS and (bottom row) flow of ZS-PECNP stabilized $scCO_2$ foams with
688 90% FQ at high superficial velocities (total 1.66 m/s).

689 Fluid leak off to the matrix from the fracture was smaller in the case of $scCO_2$ foams
690 stabilized with ZS-PECNP (Table 4). It was previously reported larger magnitude of
691 compressibility and higher apparent and dynamic viscosities prevent the fluids from
692 penetrating in pore throats of tight shale formations and help maintain a relatively high
693 internal fracture conductivity [14,59]. The volume of lost fluid to the matrix in the
694 micromodel (design #2) is related to time as [60]

695 $$\mathbf{V_L = C_w\sqrt{t} + S_P} \quad (3)$$

where V_L is the total fluid loss volume, C_W is the fluid loss coefficient and S_P is volume leaked off prior to the formation of filter cake. In micromodel tests, filter cake was neglected due to the lack of filter cake formation for foams. As a result, the following simplified relation was used for assessment, as

$$\mathbf{V_L = C_w\sqrt{t}}. \quad (4)$$

Table 4 illustrates the matrix storage capacity (portion of filled area in the matrix) and the estimated volume loss to the matrix, where the fluid loss was reduced by 11 % with ZS-PECNP $scCO_2$ foam.

Table 4. Matrix storage capacity (portion of filled area in the matrix) and the estimated volume loss for the flow into the glass micromodel.

Time (min)	Percentage of matrix filled with ZS $scCO_2$ foam (%)	Volume loss for ZS (ft^3)	Percentage of matrix filled with ZS-PECNP $scCO_2$ foam (%)	Volume loss for ZS-PECNP (ft^3)
0	80.55	1.51e-8	72.97	1.41e-8
1	88.8	1.73e-8	78.16	1.71e-8
2	88.19	1.74e-8	79.87	1.68e-8
2.5	88.49	2.04e-8	81.82	1.81e-8

Table 5 presents the values of the fluid loss coefficient for flow in glass micromodels with and for the flow through Kentucky sandstone tight core as reported in the literature: 0.18 mD permeability for Kentucky sandstone [14]. Table 5 shows the dramatic decline of fluid loss coefficient observed in microscale observations, where the fluid loss coefficient for PECNP:Surfactant mixtures is reduced by 60%.

712 Table 5. Fluid loss coefficients for measured volumes of fluid penetration into tight formation performed
713 with micro scale observations.

Stabilizing mixture	Volume loss slope ($ft^3/min^{0.5}$)	C_W ($ft/min^{0.5}$)
ZS generated $scCO_2$ foam	2.00E-08	2.39E-02
ZS-PECNP generated $scCO_2$ foam	8.00E-09	9.57E-03

714 The fluid loss coefficient is a function of FQ [58], matrix permeability,
715 surfactant/nanoparticle concentration and temperature [47]. Given constant FQ (90%),
716 temperature (40°C), and matrix permeability (see Table 1), the stabilizing mixture
717 determines the foam tendency to retain water by improving the viscosity and osmotic
718 pressure [14]. Imbibition in shale matrix of the fracturing fluid is also influenced by
719 compressibility of the rock, fracture/rock conductivity and permeability [61]. Here,
720 compressibility of complex fluids and capillary pressure in the pores controlled the amount
721 the fluids that penetrated through the pore throats of the matrix. PECNP/surfactant $scCO_2$
722 foams resulted in less pore throat plugging and damage, demonstrating yet another environment-
723 friendly aspect of waterless fracturing fluid enhanced with supercharged complexes.

724 **4. CONCLUSIONS**

725 Herein, we report the results from synergistic stabilization of $scCO_2$ in highly concentrated
726 electrolytes and corresponding fracture/matrix multiphase flow visualization in SLE fabricated
727 fused silica glass micromodels for CCUS with the potential to reduce the environmental footprint
728 of oil recovery processes. Also, we present a comparative study between micromodels fabrication
729 techniques, different ionic stabilizers and mixing phase ratios to find the optimum complex fluid
730 composition and lab-on-a-chip platform for sustainable and waterless multiphase flow in tight and
731 shale formations. The major conclusions can be summarized as follows:

1. In order to emulate a recyclable and sustainable water-less fracturing process on LOC, a zwitterionic surfactant compatible with concentrated electrolytes and charged nanoparticles was employed to interact with PECNPs electrostatically in a high salinity brine (33.3 kppm) and the mixture was co-injected with $scCO_2$ into SLE micromodels. Pre-generation of $scCO_2$ foam coupled with in-situ observation of SLE micromodel helped to identify the optimal foam quality and superficial velocities to achieve the formation of HIP with near to coarse textures and larger bubbles within the ZS generated foams. The largest detectable bubbles during the stable flow of ZS-PECNP stabilized $scCO_2$ foams were roughly 0.13x smaller and the foam had a fine-texture. The morphology and integrity of ZS-PECNP generated $scCO_2$ foams was not affected by geometrical constraints and pressure variations induced by flow divergence from micro-crack to the main fracture, whereas destabilizing effects such as bubble growth and coalescence at T-junctions were observed for ZS generated $scCO_2$ foams.

2. To characterize the dynamics of $scCO_2$ foam bubbles, dimensionless parameters containing important information about the microstructure, shear condition and relative density were calculated from macroscale observations. Laminar flow and homogenous phase dispersion were verified by the Reynolds number. Existence of hydrodynamic interactions were revealed by Peclet and low stokes value ($Stk \ll 1$), which indicated that phase segregation did not occur in the $scCO_2$ foams (FQ = 90%). Improvements in disjoining pressure through electrostatic interactions balances the forces in CO_2-water interfaces. This effect was verified by a decline of capillary number for ZS-PECNP generated $scCO_2$ foam.

3. The transport behaviour of $scCO_2$ foams enhanced with ZS and ZS-PECNP complexes in fractures was studied. Bubble population of unknown frequency was observed for ZS-PECNP generated foams because of high lamella formation and excellent stability of

electrostatically enhanced bubbles. The instability of ZS-lamella upon foam generation and isolation of $scCO_2$ bubbles led to more bubble coalescence, lamella drainage and formation of larger bubbles upon onset of mixing. On the other hand, ZS-PECNP generated $scCO_2$ foams exhibited condensed and populated arrays of smaller and monodispersed bubbles and barely recognizable midrange bubbles with sizes as big as the main fracture aperture.

4. Foam stability in fractures/micro-cracks was evaluated for a variety of stabilizing mixtures. The stability of ZS generated $scCO_2$ foams along the main fracture was negatively affected by bubble coalescence and lamella breakage. The lamella was not stable enough to separate the $scCO_2$ bubbles from each other in electrolyte solutions, whereas in ZS-PECNP generated $scCO_2$ foams, small and monodisperse droplets were largely stable in the fracture slit in the entire duration of the experiments. The stability of $scCO_2$ bubbles in the fractures were improved through the formation of electrostatically enhanced bubbles containing the aggregates of PECNP-surfactants. ZS generated $scCO_2$ foams broke into smaller bubbles confined by the micro-crack aperture. Foams within the micro-cracks were stable through the entire timeframe ($t = 2$ h) with local variations in bubble size, however, the bubbles travelled and collided into the single millimetric bubble and eventually the foam broke in the main fracture. Highly monodispersed and emulsified $scCO_2$ foam with lamella containing ZS-PECNP complexes successfully maintained their stability and offered proper channel filling due to the surfactant-brine solubility, nanoparticle compatibility to the WLMs and concentrated electrolytic interfaces.

5. An alternative design comprising a simplified two-dimensional complex flow in a matrix domain was evaluated to measure formation damage. The formation of vesicular complexes originated from electrostatic complexation of PECNP with WLMs led to stabilization

of the water-CO_2 lamella by enhancing the viscosity and osmotic pressure. The chronological binary graphs of emulated tight matrix exhibited the effective reduction of the fluid loss volume and fluid loss coefficients for PECNP:Surfactant mixtures down to 11% and 60%, respectively, by employing PECNP: surfactant which resulted in lower formation damage.

ORCID

Hooman Hosseini: 0000-0002-5072-6737

Jyun Syung Tsau: 0000-0002-1497-1911

John Wasserbauer: 0000-0002-5748-2472

Saman A. Aryana: 0000-0001-9509-7420

Reza Barati Ghahfarokhi: 0000-0002-1064-9562

ASSOCIATED CONTENT

Electronic Supporting Information (ESI) is provided by the authors. High saline brine and ZS surfactant composition, schematic of different steps in UV lithography technique, patterns used in UV lithography and SLE printing, details of image quantification, micro CT images of glass micromodels, hydraulic aperture curves, permeability calculations, notes on SLE fabrication, fused silica physical and mechanical properties, hydrodynamic and flow properties of $scCO_2$ foam, shear rate calculation in circular pipe, and chronological graphs of foam stability in fracture/matrix are presented in ESI.

AUTHOR INFORMATION

Corresponding Authors

*Reza Barati Ghahfarokhi, Department of Chemical and Petroleum Engineering, The University of Kansas, Lawrence, Kansas 66045, E-mail: reza.barati@ku.edu

Phone Number: (785)864-1232

*Saman A. Aryana, Department of Chemical Engineering, University of Wyoming, Laramie, WY 82071, USA, E-mail: saryana@uwyo.edu
Phone Number: (307) 766-1992

AUTHOR CONTRIBUTION

Conceptualization: R.G.B., H.H., S.A.A. Methodology: H.H., R.G.B., S.A.A., J.W. Software, Resources, and Investigation: S.A.A., R.G.B., H.H. Project Administration: R.G.B., S.A.A. Validation: H.H., R.B.G., S.A.A. Writing-original draft: H.H. Writing-review and editing: R.B.G., S.A.A., J.S.T., J.W., H.H. Supervision and Funding acquisition: R.G.B., S.A.A.

DISCLOSURES

There are no conflicts to declare.

ACKNOWLEDGMENT

This work was supported by the National Science Foundation EPSCor Research Infrastructure Improvement Program: Track -2 Focused EPSCoR Collaboration award (OIA- 1632892). This work was also supported as part of the Center for Mechanistic Control of Water-Hydrocarbon-Rock Interactions in Unconventional and Tight Oil Formations (CMC-UF), an Energy Frontier Research Center funded by the U.S. Department of Energy, Office of Science under DOE (BES) Award DE-SC0019165. Last but not the least, Authors gratefully acknowledge Harcros Company for providing surfactant used in this work and the authors thank Dr. Qiang (Charles) Ye for Micro-CT scanning of SLE micromodels performed at Institute for Bioengineering Research (IBER) Laboratories at University of Kansas.

ABBREVIATIONS

SLE, Selective laser induced etching; UV, Ultraviolet; $scCO_2$, supercritical CO_2; CCUS, carbon capture utilization and storage; HIP, High internal phase; VES, viscoelastic surfactant; WLM, wormlike micelle; PEI, polyethylenimine; DS, dextran sulfate; PECNP, polyelectrolyte complex nanoparticle; MLP, Mississippian limstone play; RO-DI water, reverse osmosis and deionized water; CMC, critical micelle concentration; CAD, computer aided design; IFT, interfacial tension; TDS, total dissolved solids; FQ, Foam quality; LOC, lab-on-a-chip.

REFERENCES

[1] Salisu AA, Ebuh GU, Usman N. Revisiting oil-stock nexus during COVID-19 pandemic: Some preliminary results. Int Rev Econ Financ 2020;69:280–94.

[2] Fitzgerald T. Frackonomics: some economics of hydraulic fracturing. Case W Res L Rev 2012;63:1337.

[3] Edrisi AR, Kam SI. A new foam rheology model for shale-gas foam fracturing applications. SPE Can. Unconv. Resour. Conf., Society of Petroleum Engineers; 2012.

[4] Montgomery CT, Smith MB. Hydraulic Fracturing: History Of An Enduring Technology. J Pet Technol 2010;62:26–40. https://doi.org/10.2118/1210-0026-JPT.

[5] Hosseini H, Tsau J, Peltier E, Barati R. Lowering Fresh Water Usage in Hydraulic Fracturing by Stabilizing scCO2 Foam with Polyelectrolyte Complex Nanoparticles Prepared in High Salinity Produced Water. SPE Int Conf Exhib Form Damage Control 2018. https://doi.org/10.2118/189555-MS.

[6] Yekeen N, Padmanabhan E, Idris AK. A review of recent advances in foam-based fracturing fluid application in unconventional reservoirs. J Ind Eng Chem 2018;66:45–71. https://doi.org/10.1016/j.jiec.2018.05.039.

[7] Nazari N, Hosseini H, Tsau JS, Shafer-Peltier K, Marshall C, Ye Q, et al. Development of

highly stable lamella using polyelectrolyte complex nanoparticles: an environmentally friendly scCO2 foam injection method for CO2 utilization using EOR. Fuel 2020;261:116360.

[8] Rogelj J, Den Elzen M, Höhne N, Fransen T, Fekete H, Winkler H, et al. Paris Agreement climate proposals need a boost to keep warming well below 2 C. Nature 2016;534:631–9.

[9] Rindfleisch F, DiNoia TP, McHugh MA. Solubility of polymers and copolymers in supercritical CO2. J Phys Chem 1996;100:15581–7.

[10] Sahena F, Zaidul ISM, Jinap S, Karim AA, Abbas KA, Norulaini NAN, et al. Application of supercritical CO2 in lipid extraction–A review. J Food Eng 2009;95:240–53.

[11] Mukhopadhyay M. Extraction and processing with supercritical fluids. J Chem Technol Biotechnol Int Res Process Environ Clean Technol 2009;84:6–12.

[12] Weibel GL, Ober CK. An overview of supercritical CO2 applications in microelectronics processing. Microelectron Eng 2003;65:145–52.

[13] Kankala RK, Zhang YS, Wang S, Lee C, Chen A. Supercritical fluid technology: an emphasis on drug delivery and related biomedical applications. Adv Healthc Mater 2017;6:1700433.

[14] Hosseini H, Tsau JS, Shafer-Peltier K, Marshall C, Ye Q, Barati Ghahfarokhi R. Experimental and mechanistic study of stabilized dry CO2 foam using polyelectrolyte complex nanoparticles compatible with produced water to improve hydraulic fracturing performance. Ind Eng Chem Res 2019;58:9431–49.

[15] Middleton RS, Carey JW, Currier RP, Hyman JD, Kang Q, Karra S, et al. Shale gas and non-aqueous fracturing fluids: Opportunities and challenges for supercritical CO2. Appl Energy 2015;147:500–9.

[16] Nguyen VH, Kang C, Roh C, Shim J-J. Supercritical CO2-mediated synthesis of CNT@ Co3O4 nanocomposite and its application for energy storage. Ind Eng Chem Res 2016;55:7338–43.

[17] Middleton RS, Carey JW, Currier RP, Hyman JD, Kang Q, Karra S, et al. Shale gas and non-aqueous fracturing fluids: Opportunities and challenges for supercritical CO2. Appl Energy 2015;147:500–9. https://doi.org/10.1016/j.apenergy.2015.03.023.

[18] Hosseini H, Tsau JS, Peltier E, Ghahfarokhi RB. Highly stable scCO2-high salinity brine interface for waterless fracturing using polyelectrolyte complex nanoparticles. Abstr. Pap. Am. Chem. Soc., vol. 256, AMER CHEMICAL SOC 1155 16TH ST, NW, WASHINGTON, DC 20036 USA; 2018.

[19] Hosseini H, Tsau JS, Shafer-Peltier K, Marshall C, Ye Q, Barati R. Environmentally friendly waterless fracturing with supercritical CO2 foam prepared in produced water: Mechanistic study. Abstr. Pap. Am. Chem. Soc., vol. 258, AMER CHEMICAL SOC 1155 16TH ST, NW, WASHINGTON, DC 20036 USA; 2019.

[20] Gauteplass J, Chaudhary K, Kovscek AR, Fernø MA. Pore-level foam generation and flow for mobility control in fractured systems. Colloids Surfaces A Physicochem Eng Asp 2015;468:184–92. https://doi.org/10.1016/j.colsurfa.2014.12.043.

[21] Nazari N, Tsau J-S, Barati R. CO2 Foam Stability Improvement Using Polyelectrolyte Complex Nanoparticles Prepared in Produced Water. Energies 2017;10:516. https://doi.org/10.3390/en10040516.

[22] Anandan R, Johnson S, Barati R. Polyelectrolyte Complex Stabilized CO_2Foam Systems for Hydraulic Fracturing Application. SPE Liq Basins Conf - North Am 2017:1–19. https://doi.org/10.2118/187489-MS.

892 [23] Hyman JD, Jiménez-Martínez J, Viswanathan HS, Carey JW, Porter ML, Rougier E, et al.
893 Understanding hydraulic fracturing: a multi-scale problem. Philos Trans R Soc A Math Phys
894 Eng Sci 2016;374:20150426.
895 [24] Badve M, Barigou M. Local description of foam flow, deformation and pressure drop in
896 narrow constricted channels. Int J Multiph Flow 2020:103279.
897 [25] Porter ML, Jiménez-Martínez J, Martinez R, McCulloch Q, Carey JW, Viswanathan HS.
898 Geo-material microfluidics at reservoir conditions for subsurface energy resource
899 applications. Lab Chip 2015;15:4044–53.
900 [26] Chen YF, Wu DS, Fang S, Hu R. Experimental study on two-phase flow in rough fracture:
901 Phase diagram and localized flow channel. Int J Heat Mass Transf 2018;122:1298–307.
902 https://doi.org/10.1016/j.ijheatmasstransfer.2018.02.031.
903 [27] Rognmo AU, Fredriksen SB, Alcorn ZP, Sharma M, Føyen T, Eide Ø, et al. Pore-to-Core
904 EOR Upscaling for CO 2 Foam for CCUS. SPE J 2019.
905 [28] Karadimitriou NK, Hassanizadeh SM. A review of micromodels and their use in two-phase
906 flow studies. Vadose Zo J 2012;11:vzj2011-0072.
907 [29] Elgohary A, Block E, Squier J, Koneshloo M, Shaha RK, Frick C, et al. Fabrication of
908 sealed sapphire microfluidic devices using femtosecond laser micromachining. Appl Opt
909 2020;59:9285–91.
910 [30] Hyman JD, Jiménez-Martínez J, Viswanathan HS, Carey JW, Porter ML, Rougier E, et al.
911 Understanding hydraulic fracturing: A multi-scale problem. Philos Trans R Soc A Math
912 Phys Eng Sci 2016;374. https://doi.org/10.1098/rsta.2015.0426.
913 [31] Hosseini H, Guo F, Ghahfarokhi RB, Aryana SA. Microfluidic fabrication techniques for
914 high-pressure testing of microscale supercritical CO2 foam transport in fractured

915 unconventional reservoirs. J Vis Exp 2020;2020:1–29. https://doi.org/10.3791/61369.
916 [32] Wang ZB, Guo W, Pena A, Whitehead DJ, Luk'Yanchuk BS, Li L, et al. Laser micro/nano
917 fabrication in glass with tunable-focus particle lens array. Opt Express 2008;16:19706–11.
918 [33] Yonemura M, Kato S, Hasegawa K, Takahashi H. Formation of through holes in glass
919 substrates by laser-assisted etching. J Laser Micro Nanoeng 2016;11:143–6.
920 https://doi.org/10.2961/jlmn.2016.02.0001.
921 [34] Borrelli NF, Schroeder JF, Smith CM, Streltsov A. Direct writing of optical devices in
922 silica-based glass using femtosecond pulse lasers 2005.
923 [35] Kalyanaraman N, Arnold C, Gupta A, Tsau JS, Ghahfarokhi RB. Stability improvement of
924 CO2 foam for enhanced oil-recovery applications using polyelectrolytes and polyelectrolyte
925 complex nanoparticles. J Appl Polym Sci 2017;134:1–15.
926 https://doi.org/10.1002/app.44491.
927 [36] AlQuaimi BI, Rossen WR. Study of foam generation and propagation in fully characterized
928 physical-model fracture. J Pet Sci Eng 2019;175:1169–81.
929 [37] Fernø MA, Gauteplass J, Pancharoen M, Haugen Å, Graue A, Kovscek AR, et al.
930 Experimental study of foam generation, sweep efficiency, and flow in a fracture network.
931 SPE J 2016;21:1–140.
932 [38] Burshtein N, Chan ST, Toda-Peters K, Shen AQ, Haward SJ. 3D-printed glass microfluidics
933 for fluid dynamics and rheology. Curr Opin Colloid Interface Sci 2019;43:1–14.
934 [39] Li S, Zhang S, Ma X, Zou Y, Li N, Chen M, et al. Hydraulic fractures induced by water-
935 /carbon dioxide-based fluids in tight sandstones. Rock Mech Rock Eng 2019;52:3323–40.
936 [40] Wu, X., Song, Z., Zhen, J., Wang, H., Yao, L., Zhao, M., & Dai C. A smart recyclable VES
937 fluid for high temperature and high pressure fracturing. Pet Sci Eng 2020;190:107097.

[41] Barbati AC, Desroches J, Robisson A, McKinley GH. Complex fluids and hydraulic fracturing. Annu Rev Chem Biomol Eng 2016;7:415–53.

[42] Espinosa D, Caldelas F, Johnston K, Bryant SL, Huh C. SPE 129925 Nanoparticle-Stabilized Supercritical CO 2 Foams for Potential Mobility Control Applications 2010:1–13.

[43] Anandan R, Barati R, Johnson S. Polyelectrolyte Complex Stabilized CO2 Foam Systems for Improved Fracture Conductivity and Reduced Fluid Loss 2018.

[44] Gajbhiye RN, Kam SI. Characterization of foam flow in horizontal pipes by using two-flow-regime concept. Chem Eng Sci 2011;66:1536–49. https://doi.org/10.1016/j.ces.2010.12.012.

[45] Chen L, Huang M, Li Z, Liu D, Li B. Experimental study on the characteristics of foam flow in fractures. J Pet Sci Eng 2020;185:106663.

[46] Faroughi SA, Pruvot AJCJ, McAndrew J. The rheological behavior of energized fluids and foams with application to hydraulic fracturing: Review. J Pet Sci Eng 2018;163:243–63. https://doi.org/10.1016/j.petrol.2017.12.051.

[47] Harris PC. Dynamic Fluid-Loss Characteristics of CO2-Foam Fracturing Fluids. SPE Prod Eng 1987:89–94.

[48] Zhou, Jun, P. G. Ranjith WAMW. Different strategies of foam stabilization in the use of foam as a fracturing fluid. Adv Colloid Interface Sci 2020;276:102104.

[49] Xue Z, Worthen AJ, Da C, Qajar A, Ketchum IR, Alzobaidi S, et al. Ultradry Carbon Dioxide-in-Water Foams with Viscoelastic Aqueous Phases. Langmuir 2016;32:28–37. https://doi.org/10.1021/acs.langmuir.5b03036.

[50] Green S, Walsh J, Mclennan J, Forbes B. ARMA 17-555 Hydraulic Fracture Propagation

961 in Steps Considering Different Fracture Fluids 2017:1–11.
962 [51] Palisch, T. T., Duenckel, R. J., Bazan, L. W., Heidt, J. H., & Turk GA. Determining realistic
963 fracture conductivity and understanding its impact on well performance-theory and field
964 example. SPE Hydraul. Fract. Technol. Conf., 2007.
965 [52] R. Byron Bird, Warren E. Stewart ENL. Transport Phenomena, Revised. 2nd Editio. Wiley-
966 VCH Verlag GmbH & Co.; 2006.
967 [53] Hanselmann W, Windhab E. Flow characteristics and modelling of foam generation in a
968 continuous rotor/stator mixer. J Food Eng 1998;38:393–405.
969 [54] Fei Y, Pokalai K, Johnson R, Gonzalez M, Haghighi M. Experimental and simulation study
970 of foam stability and the effects on hydraulic fracture proppant placement. J Nat Gas Sci
971 Eng 2017;46:544–54. https://doi.org/10.1016/j.jngse.2017.08.020.
972 [55] Zhu J, Yang Z, Li X, Song Z, Liu Z, Xie S. Settling behavior of the proppants in viscoelastic
973 foams on the bubble scale. J Pet Sci Eng 2019;181:106216.
974 [56] Badve M, Barigou M. Local description of foam flow, deformation and pressure drop in
975 narrow constricted channels. Int J Multiph Flow 2020:103279.
976 https://doi.org/10.1016/j.ijmultiphaseflow.2020.103279.
977 [57] Dlugogorski BZ, Schaefer TH, Kennedy EM. Verifying consistency of effective-viscosity
978 and pressure-loss data for designing foam proportioning systems. NIST SP984-3, Natl Inst
979 Stand Technol 2005.
980 [58] Wang, Jiehao DE. Fracture penetration and proppant transport in gas-and foam-fracturing.
981 J Nat Gas Sci Eng 2020:103269.
982 [59] Saldungaray PM, Palisch TT. Hydraulic fracture optimization in unconventional reservoirs.
983 SPE Middle East Unconv. gas Conf. Exhib., Society of Petroleum Engineers; 2012.

[60] Howard GC, Fast CR. Optimum Fluid Characteristics for Fracture Extension. Drill Prod Pract 1957.

[61] Gehne, Stephan PMB. Permeability enhancement through hydraulic fracturing: laboratory measurements combining a 3D printed jacket and pore fluid over-pressure. Sci Rep 2019;9:1–11.

Nomenclature

φ	gas volume fraction
V_L	fluid loss volume (ft^3)
C_w	fluid loss coefficient ($ft/min^{1/2}$)
S_P	Spurt volume (cm^3)
μ_{app}	apparent viscosity of fluids (cP)
ΔP	pressure difference read by ISCO pump (psi)
A	cross section area of the channel (cm^2)
Q	volumetric flow rate of fracturing fluid flow (cm^3/s)
k	permeability (mD)
K	flow consistency index ($Pa.S^n$)
n	flow behavior index
η	viscosity (cP)
$\dot{\gamma}$	shear rate (s^{-1})
w	Fracture width (µm)
L	Length of feature on the chip (µm)
H	Channel depth (µm)
d_H	Hydrodynamic aperture (dimensionless)

993 Graphical Abstract:

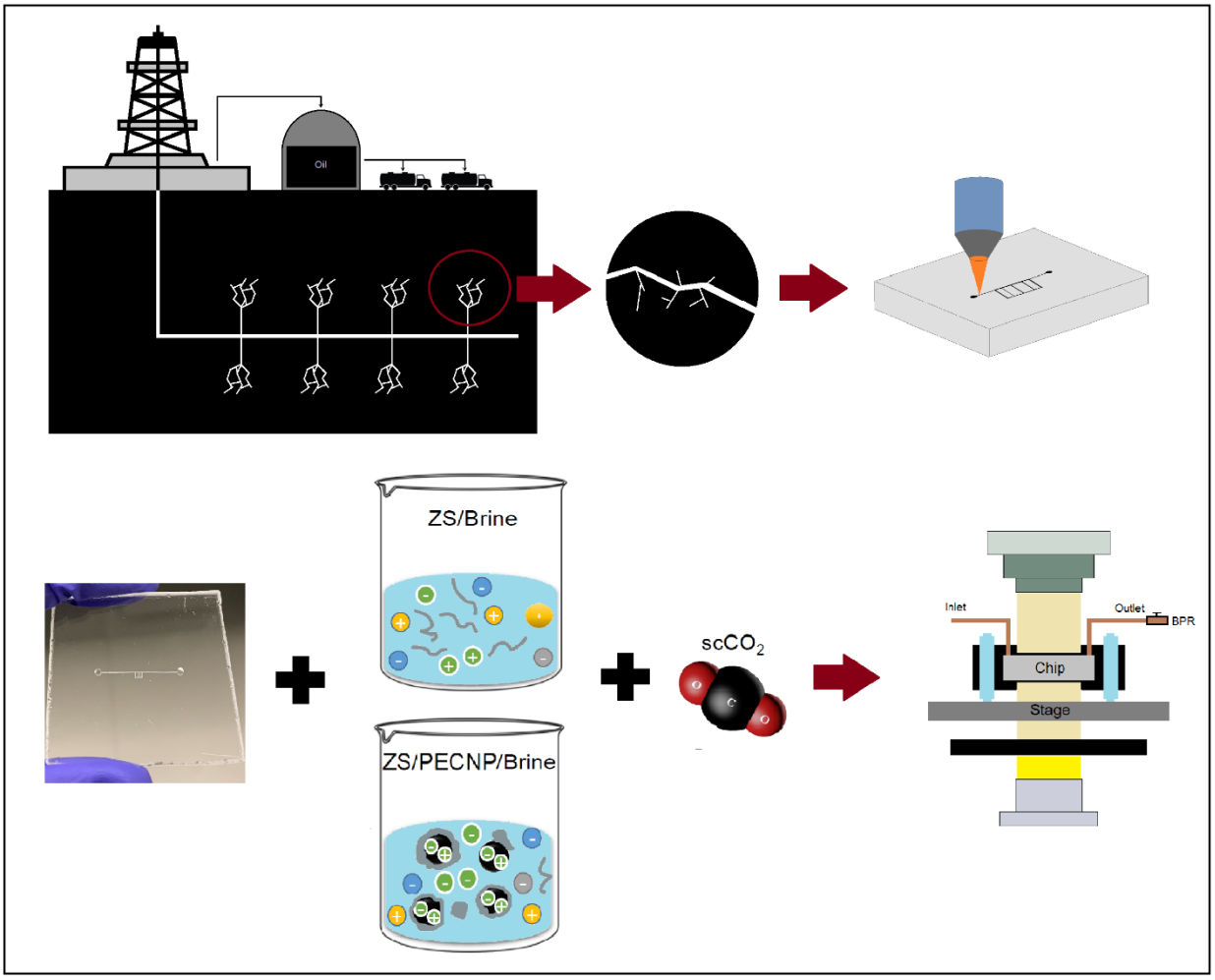

995